2013-04-19

Kinetics of Atmospheric Reactions of Biogenic Volatile Organic Compounds: Measurement of the Rate Constant of Thujone + Cl· at 296 K and Calculation ofthe Equilibrium Constant for the HO2CH2CH2O2· H2O Complex

Marie Coy Killian
Brigham Young University - Provo

Kinetics of Atmospheric Reactions of Biogenic Volatile Organic Compounds: Measurement of the Rate Constant of Thujone + $Cl^{\cdot}$ at 296 K and Calculation of the Equilibrium Constant for the $HO_2CH_2CH_2O_2 \cdot H_2O$ Complex

Marie C. Killian

A thesis submitted to the faculty of
Brigham Young University
in partial fulfillment of the requirements for the degree of

Master of Science

Jaron C. Hansen, Chair
Lee D. Hansen
Daniel E. Austin

Department of Chemistry and Biochemistry

Brigham Young University

April 2013

ABSTRACT

Kinetics of Atmospheric Reactions of Biogenic Volatile Organic Compounds: Measurement of the Rate Constant of Thujone + $Cl^{\cdot}$ at 296 K and Calculation of the Equilibrium Constant for the $HO_2CH_2CH_2O_2 \cdot H_2O$ Complex

Marie C. Killian
Department of Chemistry and Biochemistry, BYU
Master of Science

Biogenic volatile organic compounds (VOCs) react with $Cl^{\cdot}$ and $OH^{\cdot}$ radicals and the resulting radicals combine with oxygen to form peroxy radicals $RO_2^{\cdot}$. Organic peroxy radicals can then react with NO to form NO_2, a precursor of tropospheric ozone. The work presented here explored the initial reaction between $Cl^{\cdot}$ and thujone, a VOC emitted by Great Basin sagebrush. The rate constant for the reaction of thujone + $Cl^{\cdot}$ at 296 K was measured with the method of relative rates with FTIR for detection of reactants. LEDs were used to photolyze Cl_2 to generate $Cl^{\cdot}$ in the reaction cell. Thujone was also photolyzed by the LEDs and therefore the relative rates model was revised to account for this photolysis. With toluene as the reference compound, the rate constant for thujone + $Cl^{\cdot}$ at 296 K is $2.62 \pm 1.90 \times 10^{-12}$ molecules^{-1} s^{-1}, giving an atmospheric lifetime of 0.5–2.6 minutes for thujone.

Cline et al.[1] showed that the rate of the self-reaction of $HO_2CH_2CH_2O_2$ (β-HEP) increases in the presence of water vapor. This enhancement has a strong temperature dependence with a greater enhancement observed at colder temperatures. The observed rate enhancement has been attributed to the formation of a β-HEP $\cdot$ H_2O complex. In this work, the equilibrium constant for the formation of the β-HEP $\cdot$ H_2O complex was calculated by *ab initio* calculations. Given the energy available at room temperature, the complex will populate three local minimum geometries and β-HEP will populate two local minimum geometries. The partition function for each of these geometries was calculated and used to calculate the equilibrium constant for complex formation as a function of temperature. Based on these computational results, the observed temperature dependence for the rate enhancement can be attributed to the strong temperature dependence for the rate constant of the reaction of β-HEP $\cdot$ H_2O + β-HEP rather than the temperature dependence of complex formation.

Keywords: biogenic volatile organic compounds, thujone, Cl atom, relative rates, peroxy radical-water complex, $HOCH_2CH_2O_2$, β-HEP, water vapor

ACKNOWLEDGMENTS

I am grateful to all those who have supported and encouraged me in my education. My advisors, Jaron Hansen and Lee Hansen, have guided and supported me through my undergraduate and graduate work. Dr. Randy Shirts has also given extensive help in the calculations for my research. I would also like to thank my research group, especially Taylor Cline and William Keeton, for all of their help setting up the experiments and collecting data and Sambhav Kumbhani for performing the *ab initio* calculations used in my work. The BYU Chemistry department and BYU Graduate Studies have made my research possible.

Finally, I would like to thank my family who have always believed in me. My parents have always encouraged me and been there to help me when I have needed them. Most of all, I would like to thank my husband Taylor for his patience and faith in me and my daughter Anne for filling every day with joy and motivating me to reach my goals.

Table of Contents

List of Figures **vi**

List of Tables **vii**

1 Introduction **1**

1.1 National Ambient Air Quality Standards 1

1.2 Health and environmental effects of ozone 1

1.3 Health and environmental effects of particulate matter 2

1.4 Biogenic Volatile Organic Compounds 3

1.4.1 Reactions of VOCs 4

1.4.2 Particle formation 8

1.5 Oxidation of biogenic VOCs 8

1.5.1 Biogenic VOC emissions from trees 8

1.5.2 Biogenic VOC emissions from shrubs 10

1.6 Water vapor perturbation of peroxy radical reactions 14

2 Measurement of the atmospheric lifetime of thujone **16**

2.1 Relative Rates 16

2.2 Experimental methods 18

2.2.1 Reference compound 18

2.2.2 Radical source 19

2.2.3 Experimental setup and conditions 19

2.3 Results 21

3 Calculation of the equilibrium constant for β-HEP · H_2O complex formation **25**

3.1 *ab initio* calculations 26

3.2 Partition function calculations 27

3.2.1 Translational, rotational, and electronic partition functions 27

3.2.2 Vibrational partition function 29

3.3 Local minima weighting 32

3.4 Results 32

4 Conclusions and future work **49**

References **52**

A $OH^{\cdot}$ radical source **61**

B MATLAB code for relative rates experiments **62**

B.1 Reading data from *.csv files 62

B.2 Analyzing relative rates data 64

C MATLAB code for calculating the equilibrium constant for β-HEP·H_2O complex formation **68**

List of Figures

1.1 Reaction pathway of VOCs 5

1.2 Example ozone isopleth 7

2.1 The absorption profiles of thujone and toluene. 19

2.2 Diagram of reaction cell 20

2.3 Formation of HCl during the experiment 22

2.4 Reactant decays 23

2.5 Relative rates plot 24

3.1 Optimized geometries of β-HEP. 27

3.2 Optimized geometries of the β-HEP$\cdot H_2O$ complex. 28

List of Tables

3.1 β-HEP geometry 1. vibrational modes 34

3.2 β-HEP geometry 2. vibrational modes 36

3.3 β-HEP·H_2O geometry 1 vibrational modes 38

3.4 β-HEP·H_2O geometry 2 vibrational modes 41

3.5 β-HEP·H_2O geometry 3 vibrational modes 44

3.6 Results for equilibrium constant calculations with multiple vibrational models. 47

3.7 Results for equilibrium constant calculations with harmonic oscillator 48

Chapter 1

Introduction

1.1 National Ambient Air Quality Standards

Under the Clean Air Act amended in 1990, the Environmental Protection Agency (EPA) is obligated to set National Ambient Air Quality Standards (NAAQS) for six pollutants.[2] These pollutants include carbon monoxide, lead, nitrogen dioxide, ozone, particulate matter, and sulfur dioxide. Both primary and secondary standards are set for each of these pollutants. Primary standards protect public health, particularly asthmatics, children, the elderly, and other sensitive groups; secondary standards protect public welfare, including animals, plants, buildings, and visibility. Regions that fail to meet the NAAQS are declared "nonattainment areas" and are required by law to develop a plan to meet the NAAQS or face fines or loss of government funding. These plans, along with plans to maintain the air quality in regions that are in attainment, are included in State Implementation Plans (SIPs).[3] SIPs are prepared with public input and then must be approved by the state before being sent to the EPA for final review. Revisions are often necessary before a plan is approved. To develop realistic SIPs, the chemical reactions involving the six criteria pollutants must be understood, including both formation and loss mechanisms.

1.2 Health and environmental effects of ozone

Ozone, one of the EPA criteria pollutants, is a strong oxidizer, harming both human health and vegetation. Schlink et al.[4] found an increase in adverse respiratory symptoms in children when they were exposed to elevated ozone levels. Inhalation of ozone temporarily decreases

lung capacity and inflames airways, making them more reactive toward allergens.[5] The EPA characterizes the symptoms of ozone inhalation as coughing, respiratory irritation especially when breathing deeply, and shortness of breath.[6] Neural receptors in the airway stimulate these symptoms to limit the inhalation and penetration of ozone. A recent study by Fraga et al.[7] suggests that ozone exposure can induce delayed respiratory problems and that medium- to long-term effects are greater than short-term effects. Although these effects vary widely, they decrease with increasing age and decreasing body mass index.[6] Ozone may also harm the growth of lungs in children.[5] Based on a study of 95 urban communities in the United States over 13 years,[8] mortality rates increased with increased ozone levels, particularly cardiovascular and respiratory mortality.

Ozone also harms vegetation and decreases crop yield. Ozone damages the appearance of plants, decreasing the economic value, especially of horticultural crops.[9] Forest areas near large cities such as Los Angeles and Mexico City show growth decline and visible damage from elevated ozone levels.[10] Ozone slows photosynthesis and causes physical damage to the plant tissue. Avnery et al.[11] estimate that in 2000, 79–121 million metric tons of crops were lost globally to ozone damage, totaling $11–18 billion. They estimate that ozone has reduced the yield of the soybean crop by 8.5–14%, the wheat crop by 3.9–15%, and the maize crop by 2.2–5.5%. In another study, Avnery et al.[12] predict that crop yields will continue to decrease due to ozone damage, with a projected annual global loss of $12–35 billion in 2030.

1.3 Health and environmental effects of particulate matter

Particulate matter, another EPA criteria pollutant, is classified by size, usually as $PM_{2.5}$ (particulate matter with diameter <2.5 μm) or PM_{10} (particulate matter with diameter <10 μm). Although both categories of particulate matter affect human health, most recent studies focus on the health effects of $PM_{2.5}$ because of its ability to more easily enter and remain in the respiratory system. Secondary organic aerosols (SOAs) are a major source of $PM_{2.5}$. SOAs are produced when photooxidation products of organic molecules condense on the surface

of smaller particles.[13] Little work has been done to discriminate between the health effects of primary and secondary organic aerosols.[14] Exposure to $PM_{2.5}$ increases cardiovascular risk with increasing concentrations; however, no lower bound of safety has been identified.[15] $PM_{2.5}$ exposure accelerates development of cardiovascular diseases. Increased concentrations of $PM_{2.5}$ are correlated with increased incidence of cardiovascular-related problems and deaths, particularly for individuals with preexisting problems and elderly individuals, but also including those who are not critically ill.

Though the health effects of $PM_{2.5}$ are well understood, the effects of particulate matter on global climate change are more complex.[16] The direct effects of an aerosol depend on its scattering and absorbing properties. Scattering particles contribute to decreasing global temperature; whereas absorbing particles tend to contribute to cooling when over dark surfaces such as dense forests, and warming when over bright surfaces such as ice or snow. Aerosols can also act as cloud condensation nuclei, an indirect effect on global climate.

1.4 Biogenic Volatile Organic Compounds

Biogenic sources emit ≈1150 Tg of volatile organic compounds (VOCs) each year, an order of magnitude greater than anthropogenic VOC emissions.[17,18] Biogenic VOCs are generally more reactive than anthropogenically emitted VOCs.[19] Of biogenic VOC emissions, the sources can be further attributed: 821 Tg C yr^{-1} from forests, 120 Tg C yr^{-1} from crops, 194 Tg C yr^{-1} from shrubs, 5 Tg C yr^{-1} from the oceans, and 9 Tg C yr^{-1} from other biogenic sources.[17] Isoprene is the most commonly emitted biogenic VOC, accounting for nearly half of the total each year. Emissions of isoprene are light dependent and are especially common in broad leaf trees.[20] Another group of common biogenic VOCs are monoterpenes. Monoterpene emissions are temperature dependent, reflecting the increasing vapor pressure of the monoterpene with increasing temperature. Sesquiterpenes and oxygenated hydrocarbons are also emitted by many plants. Most of these biogenic VOCs are large, unsaturated molecules, suggesting high reactivity and low volatility.

1.4.1 Reactions of VOCs

Upon emission, most VOCs are oxidized, commonly by $OH^{\cdot}$, $Cl^{\cdot}$, O_3, or NO_3.[18,21] In many cases, the reactions of VOCs with $OH^{\cdot}$ and $Cl^{\cdot}$ are faster than the reactions with O_3 and NO_3. However, the reaction of VOCs with ozone can be significant if the concentration of ozone is sufficiently large compared to the concentrations of $OH^{\cdot}$ and $Cl^{\cdot}$. Reactions of VOCs with NO_3 are particularly significant in the nighttime when the concentration of NO_3 is high, in some cases exceeding the daytime concentration of $OH^{\cdot}$. Isoprene and many common monoterpenes and sesquiterpenes react with $OH^{\cdot}$, $Cl^{\cdot}$, NO_3, and O_3 with lifetimes on the order of minutes to hours, whereas lifetimes of oxygenated hydrocarbons are more variable, from hours for some compounds to as long as months or years for others. A typical reaction pathway for VOCs is shown in Figure 1.1. The initial oxidation reaction produces an alkyl radical that combines with O_2 to form a peroxy radical ($RO_2^{\cdot}$). Peroxy radicals predominantly react with each other or $HO_2^{\cdot}$ unless the concentration of NO_x is an order of magnitude greater than the concentration of peroxy radicals, in which case peroxy radicals react with NO by one of the following reactions,

$$RO_2^{\cdot} + NO \longrightarrow RO^{\cdot} + NO_2 \tag{1.1}$$

$$RO_2^{\cdot} + NO \longrightarrow RONO_2 \tag{1.2}$$

with reaction (1.1) as the major pathway. The organic nitrate formed in reaction (1.2) will eventually degrade into an alkoxy radical and NO_2, although this can take days. The NO_2 formed in reaction (1.1) is photolyzed and reacts with oxygen to produce ozone through the reactions,

$$NO_2 + h\nu \longrightarrow NO + O(^3P) \tag{1.3}$$

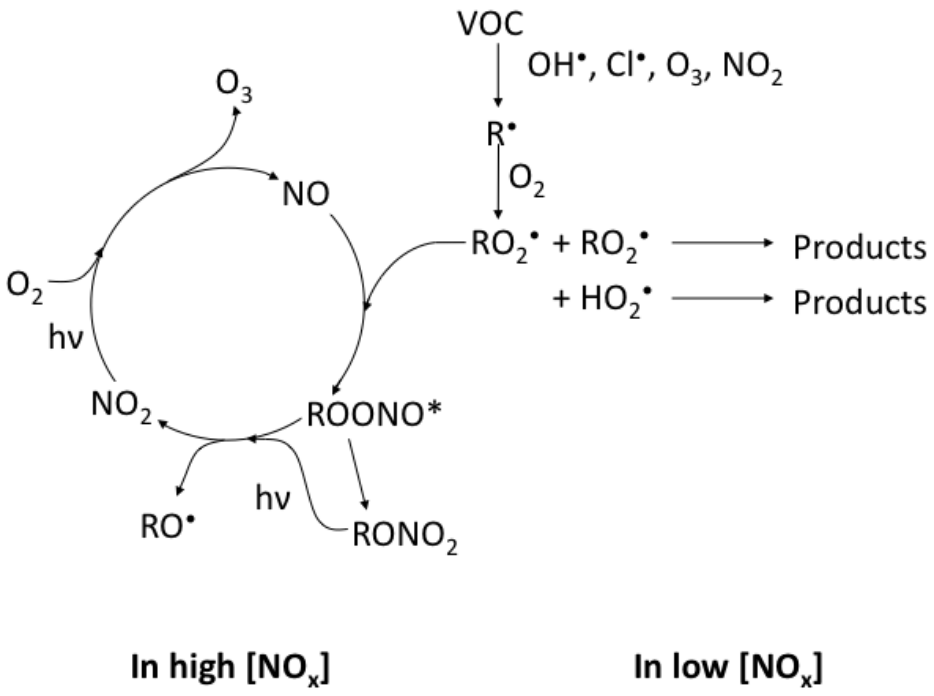

Figure 1.1: Reaction pathway of VOCs in the presence of NO_x (adapted from reference[22]).

and

$$O(^3P) + O_2 + M \longrightarrow O_3 + M^*, \tag{1.4}$$

where M is a molecule that absorbs excess energy. Ozone, in turn, reacts with NO,

$$NO + O_3 \longrightarrow NO_2 + O_2. \tag{1.5}$$

In the absence of VOCs, reactions (1.3), (1.4), and (1.5) reach a steady-state and the net concentration of ozone does not change.[22] However, even with controls on anthropogenic emissions of VOCs, biogenic emissions are abundant and uncontrolled. In the presence of VOCs, typically NO is consumed and NO_2 is produced through reaction (1.1), driving reactions (1.3) and (1.4) forward and slowing reaction (1.5). This can result in a net increase in local ozone concentration. Kumar, Prakash, and Jain[23] used urban atmospheric data to confirm that reactions (1.1), (1.2), (1.3), and (1.4) are a major atmospheric reaction pathway by demonstrating that increases in VOC concentration correspond to increases in tropospheric ozone concentration.

Ozone isopleths

The effect of varying VOC and NO_x concentrations on ozone concentrations are often depicted in ozone isopleths such as the one shown in Figure 1.2.[24] These isopleths are based on both computational modeling and experimental data. Ozone isopleths are useful in determining the potential effectiveness of VOC and NO_x controls in particular areas. For example, the ratio of VOC/NO_x is typically high in more rural areas (i.e., point A in Figure 1.2). In such regions, the ozone concentration will decrease more quickly by decreasing the concentration of NO_x than by decreasing the concentration of VOCs. Therefore, in regions with high VOC/NO_x, NO_x controls are typically more effective at reducing ozone concentrations than VOC controls. However, in regions with low VOC/NO_x ratios, characteristic of most urban areas, (point D in Figure 1.2) VOC controls are more effective at decreasing ozone concentrations. In

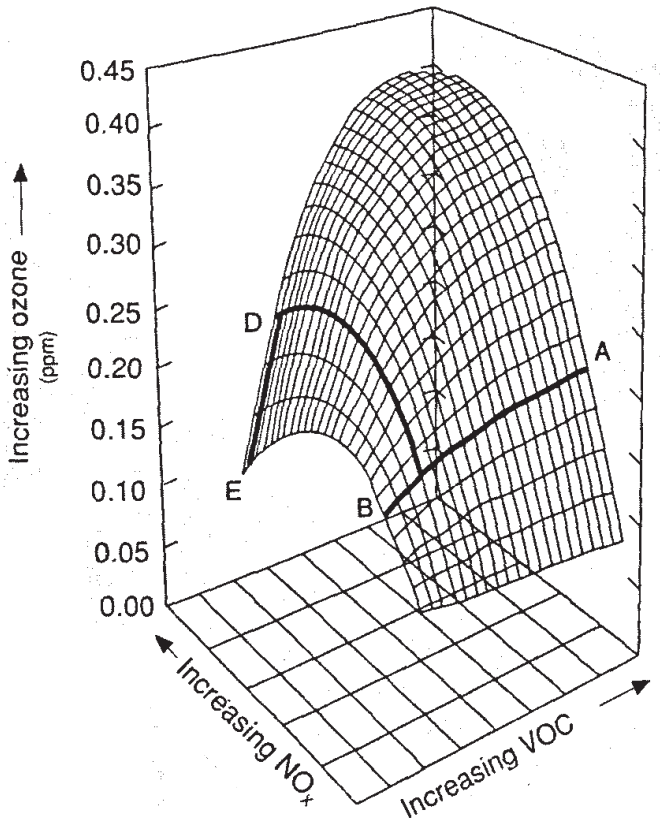

Figure 1.2: Example ozone isopleth. (Taken from Finlayson-Pitts and Pitts[25])

fact, in these areas decreasing NO_x at constant VOC can initially result in increased ozone levels until a maximum is reached and ozone concentration begins to fall with decreasing NO_x concentration. This occurs partly because, at sufficiently high NO_x concentrations, NO rapidly reacts with ozone (reaction 1.5) causing ozone levels to decrease and the reaction of NO_2 with $OH^{\cdot}$ radical competes with the reaction of VOCs with $OH^{\cdot}$, effectively slowing the formation of ozone. This behavior is reflected in the "weekend effect" observed in some urban areas where ozone concentrations increase on weekends when NO_x concentrations decrease.

1.4.2 Particle formation

The products formed when VOCs are oxidized often have low volatility. These low volatility products can form SOAs. Sjostedt et al.[26] showed that biogenic VOCs contributed significantly to the formation of SOAs in the Midwest. Tsigaridis and Kanakidou[27] estimated that biogenic VOCs contribute 2.5 to 44.5 Tg of SOAs each year, whereas anthropogenic sources contribute 0.05 to 2.62 Tg of SOAs each year. Hao et al.[28] estimated that 10 ± 2% of biogenic VOCs by mass end up contributing to SOAs. Some sources of uncertainty in these estimates include the reactions of semi-volatile oxidation products upon sticking to an aerosol and the thermodynamics of oxidation products condensing on an aerosol particle. Further, these estimates do not include the formation of SOAs from reactions of VOCs with NO_3 or $OH^{\cdot}$ or the condensation of oxidation products on existing SOAs. Therefore it is likely that these estimates are low, especially in light of recent studies[28,29] that have shown oxidation of VOCs by $OH^{\cdot}$ radical contributes significantly to particle formation. Atmospheric models currently underestimate organic aerosol mass,[30] likely in part because of the current lack of understanding of the kinetics of SOA formation from biogenic VOCs.[31]

1.5 Oxidation of biogenic VOCs

1.5.1 Biogenic VOC emissions from trees

Biogenic sources emit ≈503 Tg of isoprene each year, about 44% of total biogenic VOC emissions.[17] Although isoprene is emitted by many plants, deciduous trees emit relatively large amounts, with isoprene accounting for 78% of the total nonmethane hydrocarbon emission rate of a deciduous forest in northeastern United States.[32] As the most prevalent biogenic VOC, the atmospheric chemistry of isoprene has been extensively studied, both in the laboratory and in the field.[e.g. 17,31,33–37] Reactions with $OH^{\cdot}$ radicals and O_3 dominate isoprene chemistry during the day (with lifetimes of 1.4 hours and 1.3 days respectively), whereas during the night, reactions of isoprene with NO_3 radicals are particularly important

(lifetime of 1.6 hours).[18] The products of isoprene oxidation have been identified, with major products being formaldehyde, methacrolein, and methyl vinyl ketone for reactions with $OH^{\cdot}$ and O_3 and C_5-hydroxynitrato carbonyls or formaldehyde and C_4-nitrato carbonyls for reactions with NO_3.[38] Although isoprene oxidation products are volatile, they have recently been found to contribute to SOAs.[31] Hoyle et al.[37] estimate that isoprene oxidation products contribute about 15 Tg yr^{-1} of SOAs, or about 27% of the total SOAs formed.

Monoterpenes are another major type of biogenic VOC, comprising about 11% of the global biogenic VOC emission.[17] α- and β-pinene are the most abundantly emitted monoterpenes, with emissions of 4.5 and 3.2 Tg C yr^{-1} respectively.[39] Both α- and β-pinene are emitted by most trees and plants to varying degree, being most abundantly emitted by coniferous trees.[40] The southeastern United States, Pacific Coast, and many of the coniferous forests in the western United States are dominated by emissions of α- and β-pinene. The lifetimes of α-pinene in the presence of $OH^{\cdot}$, O_3, and NO_3 are 2.6 hours, 4.6 hours, and 11 minutes respectively.[18] The products of these reactions include pinonaldehyde, acetone, and formaldehyde. The lifetimes of β-pinene in the presence of $OH^{\cdot}$, O_3, and NO_3 are 1.8 hours, 1.1 days, and 27 minutes respectively. The products of these reactions include nopinone, formaldehyde, and acetone. The oxidation products of both α- and β-pinene have potential to form SOAs.[41,42] With high reactivity and emission rates, α- and β-pinene are significant factors in the atmospheric chemistry of regions dominated by coniferous forests.

Emissions from coniferous forests also contain d-limonene, myrcene, and Δ^3-carene depending on the particular species of trees that dominate the area.[40] Deciduous forests emit a greater variety of monoterpenes, but in lesser abundance, including α- and β-pinene, Δ^3-carene, sabinene, β-phellandrene, ρ-cymene, and ocimene. The northern boreal forest region emits a relatively even mix of α- and β-pinene, Δ^3-carene, myrcene, and camphene. The atmospheric lifetimes of each of these compounds has been measured.[18,43] In addition, the potential of monoterpenes to form SOAs is being studied, with both isolated monoterpenes and mixtures of emissions from plants.[e.g. 28,29,44,45]

1.5.2 Biogenic VOC emissions from shrubs

The emission profile of shrubs and the reactions of the VOCs emitted by shrubs have received much less attention than VOCs emitted by trees. In a review of biogenic VOCs, including their origins and reactions, Fuentes et al.[20] state that the VOCs emitted from shrubs are "very poorly characterized." Although the biomass of many shrubs is less than the biomass of trees, their potential atmospheric impact is still significant. Arey et al.[46] reported that California sagebrush had nearly twice the estimated emission rates per gram of dry leaf of any other plants in the region including oak and fir trees. However, they note that the observed rates are dependent on measurement technique and because these measurements were performed on potted, transplanted plants, they may not be representative of undisturbed plants. Guenther et al.[17] estimated that shrubs are responsible for approximately 17% of biogenic VOC emissions. Emission rates of shrubs are often correlated with moisture and growth[47] and have been shown to increase when the plant is physically damaged.[48,49] A study by Geron et al.[50] suggests that plants common in desert ecosystems have significantly lower emissions of isoprene than deciduous and coniferous tress. However, emissions of monoterpenes and oxygenated compounds from desert plants are significant.

In 1999, Diem[47] studied ozone concentrations in Tucson as a function of time. The "weekend effect," where ozone concentrations are highest on weekends, is associated with an environment where ozone formation is dependent on VOC concentrations (see section 1.4.1). Conversely, the "weekday effect" is associated with NO_x-sensitive ozone production. In April, only the downtown monitor demonstrated the "weekend effect," suggesting high concentrations of VOCs. During April, many native plants are at the peak of their blooming, a process that can increase biogenic VOC emissions.[17] Therefore it is likely that areas outside of downtown are rich in VOCs during April, suggesting that biogenic sources are the driving source of VOCs in ozone formation in Tucson.[47] The arid foresummer then set in and during June, most of the area experienced the "weekend effect," or low VOC/NO_x ratios, and then in July all monitoring stations reported the "weekday effect," or NO_x-sensitve ozone production.

This shift reflects the onset of the North American Monsoon, a time of increased moisture and likely increased emissions of biogenic VOCs.

A recent study by Sorooshian[51] gives evidence that biogenic VOCs in southern Arizona significantly contribute to aerosols in this region, particularly during the monsoon season. The emissions of desert plants include oxygenated isoprenoids and sesquiterpines,[52] compounds that have particularly high potential to form SOAs.[51,53] Matsunaga et al.[54] identified salicylic esters as biogenic VOCs emitted at high rates from some desert plants. They predict that these emissions likely contribute substantially to the concentration of SOAs in desert regions.

According to Küchler vegetation types, shrub-dominated land covers 1,517,328 km^2 or 33.1% of the conterminous western United States (defined as Arizona, California, Colorado, Idaho, Kansas, Montana, Nebraska, Nevada, New Mexico, North Dakota, Oklahoma, Oregon, South Dakota, Texas, Utah, Washington, and Wyoming).[55] Some of the desert shrub types most prominent in Utah, Nevada, Arizona, and California are characterized by sagebrush (*Artemisia*), saltbush-greasewood (*Atriplex-Sarcobatus*), and creosotebush (*Larrea*). The Great Basin sagebrush vegetation type covers 169,959 km^2 of the western states and sagebrush partly characterizes the sagebrush steppe which covers another 370,208 km^2. Saltbush-greasewood vegetation type covers 157,024 km^2 of the western states and vegetation types characterized by creosotebush cover 135,857 km^2 of the western states. These three plant types have been included in some emission studies summarized in following pages.

Many of the VOCs emitted by desert shrubs are common with the VOC emissions of forests. As described in section 1.5.1, the atmospheric lifetimes of many of these biogenic VOCs have been measured. However, some of the emissions by desert plants are unique and have not been previously studied for their atmospheric reactivity. These emissions include thujone, artemiseole, artemisia alcohol, α-terpineol, and homosalate. In this work, the kinetics of the reaction of thujone with $Cl^{\cdot}$ radical were measured by the relative rate method and with an FTIR detection scheme. $Cl^{\cdot}$ atoms were used in the thujone relative rates experiment because of spectral interferences of the $OH^{\cdot}$ radical precursor. Although $Cl^{\cdot}$ has

traditionally been considered relatively unique to coastal regions, a recent study by Thornton et al.[56] reported high concentrations of $ClNO_2$, a source of $Cl^{\cdot}$, in the mid-continental United States. Both $OH^{\cdot}$ and $Cl^{\cdot}$ typically abstract hydrogens from the alkyl chains of ketones such as thujone and consequently $Cl^{\cdot}$ can be used as a surrogate for understanding $OH^{\cdot}$ radical reactions.[57]

Great Basin sagebrush

Arey et al.[46] found that emissions from California Sagebrush (*Artemisia californica*) varied significantly between specimens, but averaged 47±19 μg g^{-1} h^{-1}, though this value may have been affected by measurement technique. The major emissions identified included artemisia ketone, artemisia alcohol, α- and β-thujone, 1,8-cineole, camphor, and some monoterpenes and sesquiterpenes. Two later studies[48,49] identified some VOC emissions from sagebrush and measured the changes in VOC emissions with physical damage (typically caused by animals). Preston, Laue, and Baldwin[49] identified cineole, thujone, and camphor as major emissions from *Artemisia tridentata* and methyl jasmonate as a minor emission and possible airborne signal. Kessler et al.[48] identified major emissions as β-pinene, artemiseole, 1,8-cineole, (E)-2-hexenal, p-cymene, cis-3-hexenyl acetate, cis-3-hexenol, and camphor and left several emissions unidentified. Emissions of all measured compounds increased by at least two-fold with physical damage.

Saltbush-greasewood

In a study of three sites in the United States, Helmig et al.[58] identified VOC emissions from the major vegetation types in each area. Near Hayden, CO, saltbush was identified as a "high emitter," emitting about 48 μg C h^{-1} gdw^{-1} (gdw = gram dry weight). Major identified emissions included acetone (1.6 μg C h^{-1} gdw^{-1}), an isomer of dimethylfuranone (1.5 μg C h^{-1} gdw^{-1}), α-pinene (15 μg C h^{-1} gdw^{-1}), β-pinene (1.3 μg C h^{-1} gdw^{-1}), cis-3-hexenyl

acetate (2.0 μg C h^{-1} gdw^{-1}), p-cymene (3.4 μg C h^{-1} gdw^{-1}), d-limonene (2.2 μg C h^{-1} gdw^{-1}), and α-terpineol (1.1 μg C h^{-1} gdw^{-1}).

Creosotebush

Because of the evidence for biogenic VOC emissions contributing to ozone formation found by Diem[47] (see section 1.5.2), Jardine et al.[52] began an effort to quantify the VOCs emitted by creosotebush, particularly *Larrea tridentata*, a plant common to the three warm deserts in North America. Data were collected during the summer months to include the monsoon season. They identified a wide variety of oxygenated biogenic VOCs, sulfides, nitriles, and fatty acid oxidation products, several of which are not commonly observed in forested areas. Further, several aromatic VOCs were identified, a class of compounds commonly associated with anthropogenic emissions. Some of the major emissions identified include isoprene (7.5 $\pm$ 7.8 μg C h^{-1} gdw^{-1}), monoterpenes (10.4 $\pm$ 9.6 μg C h^{-1} gdw^{-1}), methanol (4.5 $\pm$ 4.1 μg C h^{-1} gdw^{-1}), acetaldehyde (3.7 $\pm$ 3.2 μg C h^{-1} gdw^{-1}), ethanol (11.1 $\pm$ 7.9 μg C h^{-1} gdw^{-1}), acetone (2.5 $\pm$ 2.1 μg C h^{-1} gdw^{-1}), acetic acid (1.7 $\pm$ 0.9 μg C h^{-1} gdw^{-1}), 2,4-dithiapentane (1.2 $\pm$ 0.6 μg C h^{-1} gdw^{-1}), and homosalate (3.5 $\pm$ 3.1 μg C h^{-1} gdw^{-1}). All compounds identified were also detected in the surrounding atmosphere.

An earlier study of the emissions of creosotebush[50] measured monoterpene emissions at a rate of about 2 μg C g^{-1} h^{-1}. They identified *d*-limonene, α-pinene, and camphene as dominant monoterpene emissions and β-pinene, myrcene, and γ-terpinene as other emissions. $Z-\beta$-ocimene was measured in high abundance in the absence of ozone. They also measured β-caryonphylene, a sesquiterpene, emitted at rates from 0.5 to 2 μg C g^{-1} h^{-1}. Other emissions identified include 2-ethyl-1-hexanol, oxygenated terpenoids, acetaldehyde, methanol and ethanol.

1.6 Water vapor perturbation of peroxy radical reactions

Organic peroxy radicals ($RO_2^{\cdot}$) are intermediates in the oxidation of hydrocarbons as shown in Figure 1.1. When the concentration of NO_x is an order of magnitude greater than total $RO_2^{\cdot}$ concentration, peroxy radicals react predominantly with nitric oxide (NO). But when the concentration of NO_x is within an order of magnitude of the total $RO_2^{\cdot}$ concentration, the peroxy radical self-reaction or reaction with $HO_2^{\cdot}$ or other peroxy radicals becomes important. All of these reactions can perturb tropospheric ozone production.[21]

In 1975, Hamilton[59] discovered that water vapor enhances the self-reaction rate of $HO_2^{\cdot}$, the most concentrated peroxy radical in earth's atmosphere. He attributed this enhancement to the formation of an $HO_2 \cdot H_2O$ complex. Since then, numerous studies have verified the enhancement and confirmed the formation of the complex.[e.g. 60–65] The experimental evidence indicates that formation of a water-radical complex alters the energy barriers of radical reactions and is responsible for the observed rate increase.[66–69]

Computational work[70] indicates that alkylperoxy radicals can also complex with water vapor and therefore reaction rates involving these radicals may be dependent on water vapor. Cline et al.[1] measured the water vapor enhancement of the self-reaction of β-hydroxyethylperoxy radical ($HOCH_2CH_2O_2^{\cdot}$ or β-HEP) and found the observed rate as much as doubled in high humidity at low temperatures. However, English et al.[67] found that water vapor did not significantly affect the self-reaction of $CH_3O_2^{\cdot}$, which they attributed to the low binding energy and small fraction of $CH_3O_2^{\cdot}$ that complexes with water at atmospheric conditions. At 100% relative humidity, only 0.02-0.05% of $CH_3O_2^{\cdot}$ is complexed with water, whereas 7.8-15% of $HO_2^{\cdot}$ molecules are complexed under the same conditions.[67,71] A computational study[70] predicts that β-HEP forms a strong complex with water (5.9 kcal mol^{-1}) comparable to the complex formed by $HO_2^{\cdot}$ and H_2O (6.9 kcal mol^{-1})[72] and stronger than the binding energy of $CH_3O_2^{\cdot}$ and water, 2.4 kcal mol^{-1}.[70] The equilibrium constant for the complex formation has an exponential term that includes this binding energy, exaggerating the effects of these differences in binding energies on the amount of complex formed. β-HEP

is formed from oxidation of ethylene, a ripening agent of vegetation as well as a product of fossil fuel and wood combustion. Total annual global emissions of ethylene are estimated to be 18–45 Tg.[73]

In this work, the equilibrium constant for the formation of the β-HEP·H_2O complex is calculated with high level *ab initio* calculations. The equilibrium constant is then used to estimate the percent of β-HEP that is complexed with water under the experimental conditions used by Cline et al.[1]

Chapter 2

Measurement of the atmospheric lifetime of thujone

2.1 Relative Rates

Directly measuring reaction rates involving radicals can be difficult because radicals are short-lived and must be created and then measured in situ. These constraints introduce large uncertainties in measured concentrations of radicals. The method of relative rates is commonly used to eliminate the need to measure the absolute radical concentration in experiments to determine the kinetics of radical reactions.[74] Further, with this method, experiments can be performed with low reactant concentrations and high overall pressure, conditions present the atmosphere. In the relative rates method, the reactions of two compounds, X_1 and X_2, with a radical (such as $Cl^{\cdot}$ in this study) are monitored simultaneously, where the reaction of X_1 with $Cl^{\cdot}$ is the reaction of interest and the reaction of X_2 with $Cl^{\cdot}$ has previously been studied and the rate constant is known. The rate laws for the two reactions,

$$X_1 + Cl \longrightarrow P_1 \tag{2.1}$$

and

$$X_2 + Cl \longrightarrow P_2 \tag{2.2}$$

are

$$\frac{d[X_1]}{dt} = -k_1[X_1][Cl] \tag{2.3}$$

and

$$\frac{d[\mathrm{X_2}]}{dt} = -k_2[\mathrm{X_2}][\mathrm{Cl}] \tag{2.4}$$

Equations (2.3) and (2.4) can be rearranged to

$$-\frac{d\ln[\mathrm{X_1}]}{dt} = k_1[\mathrm{Cl}] \tag{2.5}$$

and

$$-\frac{d\ln[\mathrm{X_2}]}{dt} = k_2[\mathrm{Cl}] \tag{2.6}$$

which can be combined to

$$-\frac{1}{k_1}\frac{d\ln[\mathrm{X_1}]}{dt} = -\frac{1}{k_2}\frac{d\ln[\mathrm{X_2}]}{dt} \tag{2.7}$$

By integrating each side of equation (2.7) from time = 0 to time = t, we get the expression,

$$\ln\frac{[\mathrm{X_1}]_0}{[\mathrm{X_1}]_t} = \frac{k_1}{k_2}\ln\frac{[\mathrm{X_2}]_0}{[\mathrm{X_2}]_t} \tag{2.8}$$

Because both hydrocarbons, $\mathrm{X_1}$ and $\mathrm{X_2}$, are exposed to the same concentrations of radical at all times, the concentration of radical cancels and the measured ratio of rate constants is independent of radical concentration. The rate constant of reaction 2.1, k_1, can then be determined by plotting $\ln\frac{[\mathrm{X_1}]_0}{[\mathrm{X_1}]_t}$ against $\ln\frac{[\mathrm{X_2}]_0}{[\mathrm{X_2}]_t}$ and fitting with a linear regression. The slope from the regression is the ratio, $\frac{k_1}{k_2}$, and using the known value of k_2, k_1 is determined.

A common method for producing the radical involves photolyzing a precursor compound. Because this must be done in the reaction cell, the hydrocarbons are also exposed to the photons and therefore may be photolyzed as well. The reference hydrocarbon can be chosen such that it does not significantly absorb at the wavelengths used. However, in this experiment, thujone ($\mathrm{X_1}$) is photolyzed by the light used to generate the radical ($\approx$375 $\pm$ 10 nm). This photolysis can be included in the relative rates model by the following revisions. If $\mathrm{X_1}$ is being photolyzed as well as reacting with $\mathrm{Cl^{\cdot}}$, the expression for loss of $\mathrm{X_1}$ over time

(equation (2.3)) becomes

$$\frac{d[\mathrm{X_1}]}{dt} = -k_1[\mathrm{X_1}][\mathrm{Cl}] - \mathcal{F}\sigma\Phi[\mathrm{X_1}] \tag{2.9}$$

where $\mathcal{F}$ is the photon flux, σ is the absorption cross section of $\mathrm{X_1}$ at the wavelengths used, and Φ is the quantum yield of the photolysis at those wavelengths. Including this expression for the loss of $\mathrm{X_1}$, equation (2.7) becomes

$$-\frac{1}{k_1}\frac{d\ln[\mathrm{X_1}]}{dt} - \frac{\mathcal{F}\sigma\Phi}{k_1} = -\frac{1}{k_2}\frac{d\ln[\mathrm{X_2}]}{dt} \tag{2.10}$$

and the expression used to fit the data (equation 2.8) is now,

$$\ln\frac{[\mathrm{X_1}]_0}{[\mathrm{X_1}]_t} = \frac{k_1}{k_2}\ln\frac{[\mathrm{X_2}]_0}{[\mathrm{X_2}]_t} + \mathcal{F}\sigma\Phi t \tag{2.11}$$

Therefore by fitting $\ln\frac{[\mathrm{X_1}]_0}{[\mathrm{X_1}]_t}$ to a multivariable linear regression with $\ln\frac{[\mathrm{X_2}]_0}{[\mathrm{X_2}]_t}$ as one independent variable and t as the other, the slope for $\ln\frac{[\mathrm{X_2}]_0}{[\mathrm{X_2}]_t}$ will again be the ratio, $\frac{k_1}{k_2}$, and the slope for t will be $\mathcal{F}\sigma\Phi$.

2.2 Experimental methods

2.2.1 Reference compound

In order to minimize uncertainty, the rate constant of the reference compound with the radical should be within an order of magnitude of the rate constant being measured (i.e. 0.1 $<\frac{k_1}{k_2}<$10). Further, when FTIR spectroscopy is used as the detection scheme, the reference compound must exhibit unique absorption features, allowing its concentration to be monitored independently from thujone. Toluene was used as the reference compound for thujone because the absorption profiles of thujone and toluene allow both to be monitored independently (see Figure 2.1), and the rate constant for the reaction of toluene with $\mathrm{Cl}^{\cdot}$ is well known[75] and within an order of magnitude of the rate constant for the reaction of thujone with $\mathrm{Cl}^{\cdot}$.

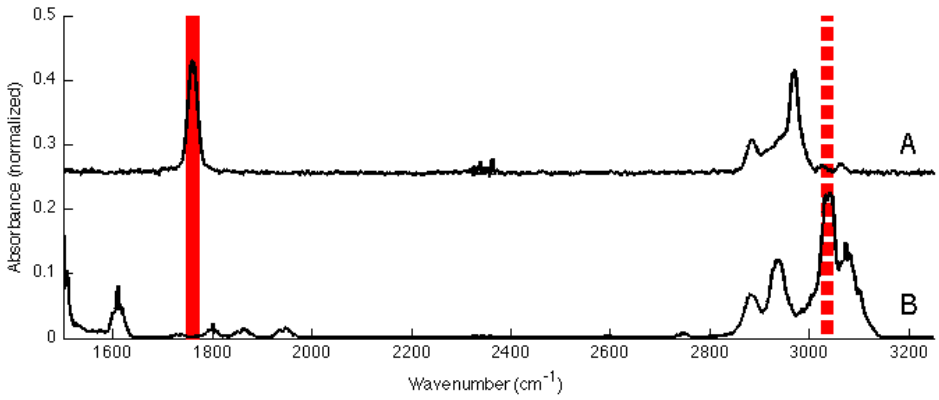

Figure 2.1: The absorption profiles of thujone and toluene. The region used to monitor the concentration of thujone is indicated by a solid line (between 1757 cm^{-1} and 1767 cm^{-1}) and the region used to monitor toluene is indicated by a dotted line (between 3032 cm^{-1} and 3042 cm^{-1}).

2.2.2 Radical source

In this study, the reaction kinetics of thujone with Cl$^{\cdot}$ atom were measured. Cl$^{\cdot}$ atoms were produced in the cell by photolyzing Cl_2 gas (4.975%, purchased from Air Liquide) with 375 nm light. Chlorine gas does not absorb in the IR and therefore cannot mask the absorption features of thujone or toluene.

2.2.3 Experimental setup and conditions

The experiment was performed with a Thermo Nicolet Nexus 670 FTIR spectrophotometer. The instrument collected spectra with 0.25 cm^{-1} resolution and averaged 16 scans for each spectrum. The gases were contained in a glass cell about 19 cm long and 4 cm in diameter. The IR beam passed through sodium chloride windows placed on the ends of the cell. The cell was surrounded by four banks of 13 LEDs that emit 375 nm light. The center wavelength for the LED emission is 375 $\pm$ 10 nm with a full width half maximum of 10 nm.[76] A diagram of the reaction cell is given in Figure 2.2.

Approximate partial pressures of the gases in the cell were: 3 Torr thujone ($\geq$ 65%, Sigma Aldrich), 10 Torr toluene, 20 Torr Cl_2, and then filled to about 200 Torr with N_2. The

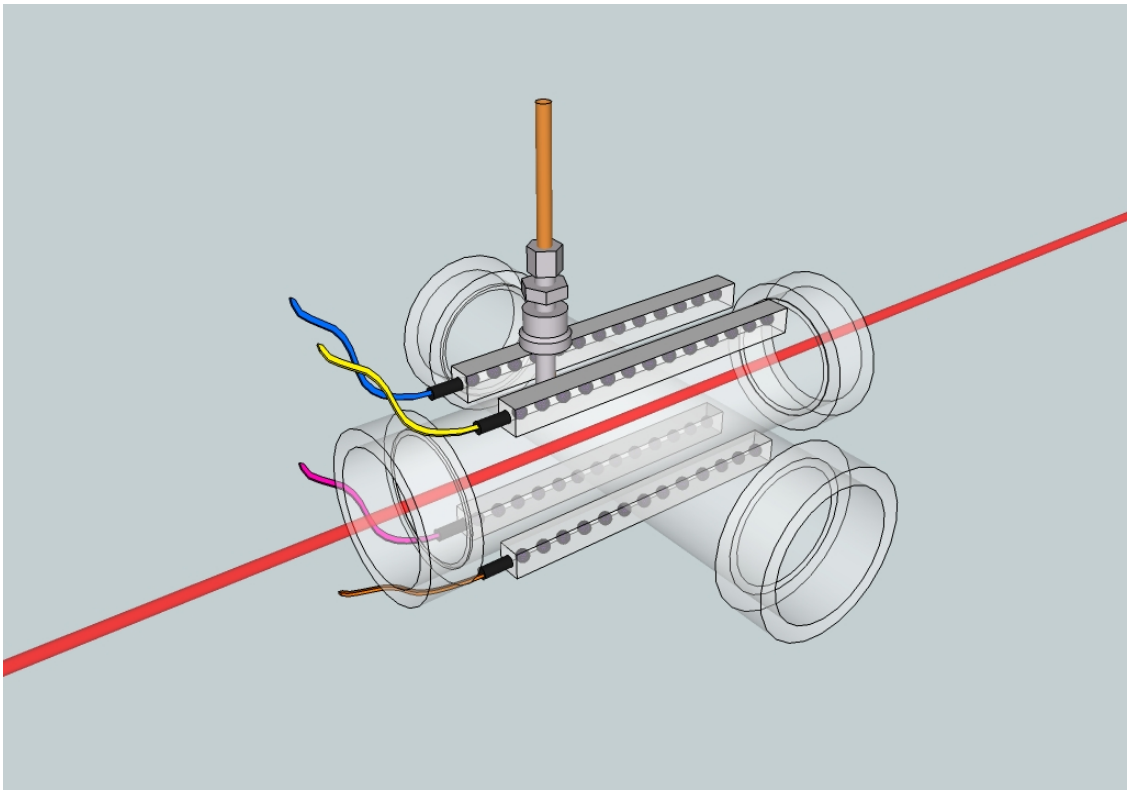

Figure 2.2: The reaction cell is surrounded by four banks of LEDs to photolyze the radical precursor.

precise concentration of each reactant is not needed in the analysis because only the ratio of initial concentration to concentration at each time is used.

Water lines appeared in the IR spectrum due to impurities in the thujone and nitrogen gas. Although anhydrous sodium sulfate was added to the thujone solution and the nitrogen passed through a drying stage, the water could not be removed completely. The wavelengths where these water lines occurred were not used in any quantitative measurement.

During each experiment, spectra were collected about every 6 minutes for about 13 hours. For analysis, the data were truncated at 5400 seconds (90 minutes or 16 data points) because the decays began to flatten and secondary chemistry began to interfere. The concentration of each compound was monitored by taking the average absorption of thujone between 1757 cm^{-1} and 1767 cm^{-1} (excluding the data between 1761 cm^{-1} and 1763 cm^{-1} because of interference by water) and the average absorption of toluene between 3032 cm^{-1} and 3042 cm^{-1}. These ranges are indicated on the spectra in Figure 2.1. The data point for the initial concentration was taken as the first spectrum taken after both thujone and toluene had reached a maximum concentration.

2.3 Results

The MATLAB code used to analyze the relative rates data is included in the Appendix (see Appendix A). Figure 2.3 shows the formation of HCl over time as the $Cl^{\cdot}$ atoms abstract a hydrogen atom from the thujone and toluene. The rate constant for the reaction of toluene + Cl is $5.89 \pm 0.36 \times 10^{-12}$ cm^3 $molecules^{-1}$ s^{-1} at 296 K.[75] Example decays of thujone and toluene over time are shown in Figure 2.4.

An example plot of $\ln \frac{[X_1]_0}{[X_1]_t}$ against $\ln \frac{[X_2]_0}{[X_2]_t}$ with toluene as the reference compound is shown in Figure 2.5. The figure also shows both the basic relative rates fit (equation (2.8), –) and the multivariate fit that corrects for the photolysis of thujone (equation (2.11), – –). The rate constant for the reaction of thujone + Cl was measured to be $2.62 \pm 1.90 \times 10^{-12}$ $molecules^{-1}$ s^{-1} at 296 K with toluene as the reference compound. The uncertainty is taken

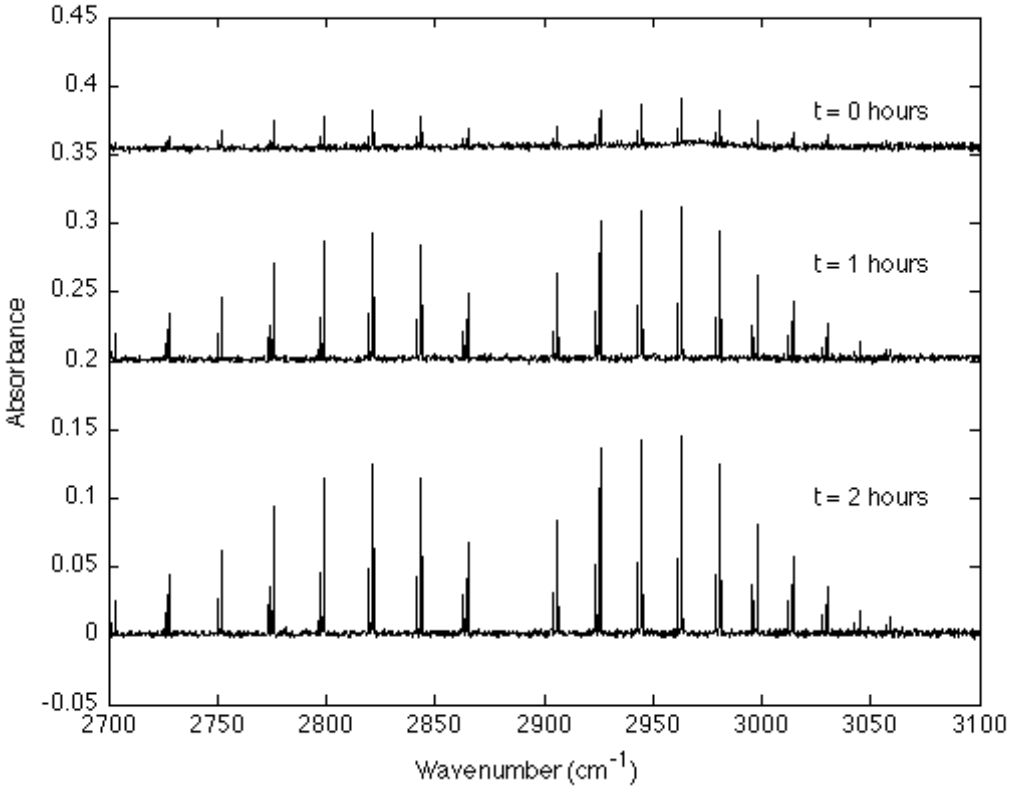

Figure 2.3: When Cl˙ reacts with thujone and toluene it abstracts a hydrogen atom to form HCl. The spectra in this figure show the increase in HCl concentration over the course of the experiment.

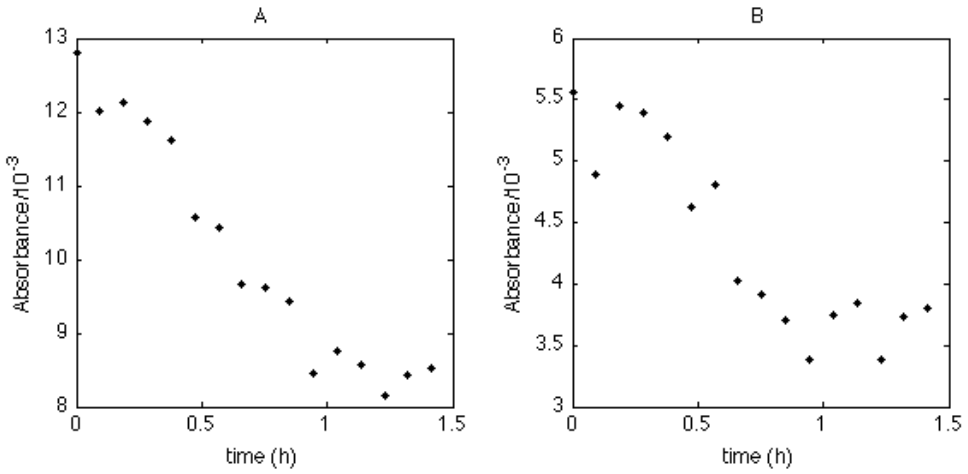

Figure 2.4: Decays of the absorption peak of thujone in A and toluene in B.

as two times the standard deviation of the rate constants from the eleven trials, including the propagation of the uncertainty in the toluene rate constant. The basic relative rates model that does not include the photolysis of thujone gives the rate constant for thujone + $Cl^{\cdot}$ as $3.88 \pm 3.40 \times 10^{-12}$ molecules^{-1} s^{-1}. Therefore, without the correction for photolysis, the rate constant is overestimated by a factor of 1.5 and greater uncertainty is observed. Based on an average $Cl^{\cdot}$ concentration of 100–500 pptv,[56] the atmospheric lifetime of thujone in the presence of $Cl^{\cdot}$ is 0.5–2.6 minutes.

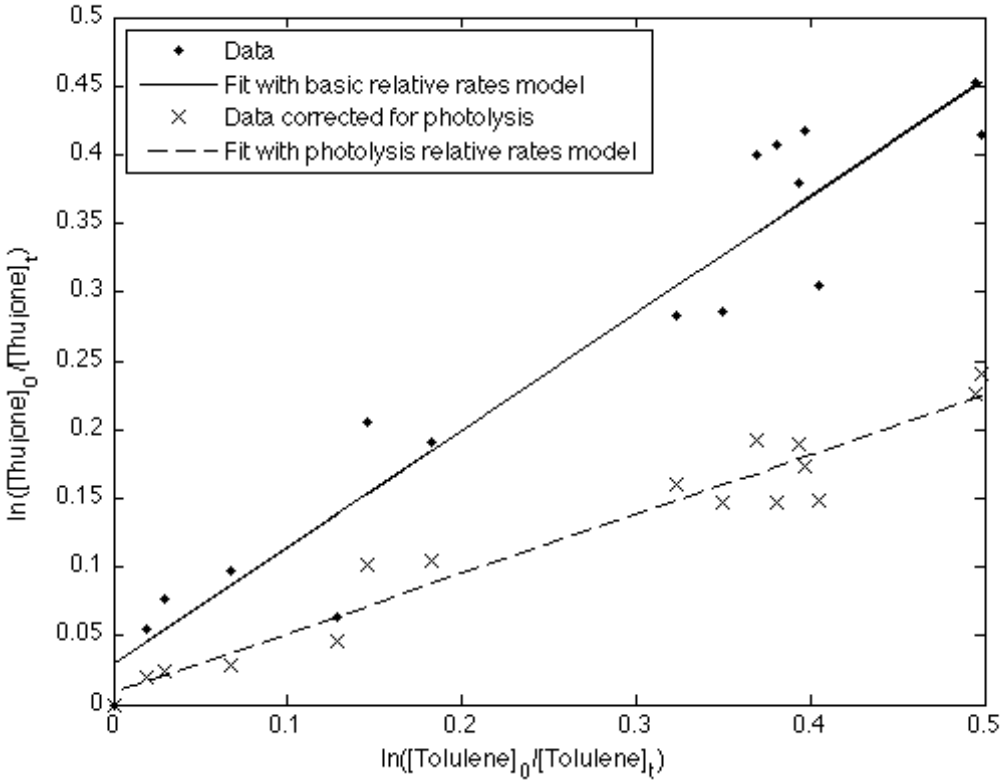

Figure 2.5: Plot of ln $\frac{[thujone]_0}{[thujone]_t}$ against ln $\frac{[toluene]_0}{[toluene]_t}$ ($\bullet$) with the basic relative rates fit (–) and the data corrected for photolysis, ln $\frac{[thujone]_0}{[thujone]_t} - \mathcal{F}\sigma\Phi t$, against ln $\frac{[toluene]_0}{[toluene]_t}$ ($\times$) with the fit to the photolysis–corrected relative rates model (– –).

Chapter 3

Calculation of the equilibrium constant for β-HEP $\cdot$ H_2O complex formation

Cline et al.[1] measured the rate constant for the self-reaction of β-hydroxyethylperoxy radical (β-HEP) in the presence of water vapor. The observed rate constant is for a combination of the following reactions,

$$HOCH_2CH_2O_2 + HOCH_2CH_2O_2 \longrightarrow \text{Products} \tag{3.1}$$

$$HOCH_2CH_2O_2 + H_2O \rightleftharpoons HOCH_2CH_2O_2 \cdot H_2O \tag{3.2}$$

$$HOCH_2CH_2O_2 \cdot H_2O + HOCH_2CH_2O_2 \longrightarrow \text{Products} \tag{3.3}$$

$$HOCH_2CH_2O_2 \cdot H_2O + HOCH_2CH_2O_2 \cdot H_2O \longrightarrow \text{Products} \tag{3.4}$$

The total loss of β-HEP (both uncomplexed and complexed radicals) was measured as a function of time. The total loss of β-HEP can be expressed by the following rate equation,

$$\begin{aligned} \frac{d[\text{HEP} + \text{HEP} \cdot H_2O]}{dt} &= -2k_{obs}\left([\text{HEP}] + [\text{HEP} \cdot H_2O]\right)^2 \\ &= -2k_{3.1}[\text{HEP}]^2 + 2k_{3.3}[\text{HEP}][\text{HEP} \cdot H_2O] \\ &\quad - 2k_{3.4}[\text{HEP} \cdot H_2O]^2 \end{aligned} \tag{3.5}$$

k_{obs} is a function of rate constants, the equilibrium constant for complex formation (K), and water concentration,

$$k_{obs} = \frac{k_{3.1} + k_{3.3}K[\mathrm{H_2O}] + k_{3.4}K^2[\mathrm{H_2O}]^2}{(1 + K[\mathrm{H_2O}])^2} \tag{3.6}$$

This expression can be simplified because the value of $K[\mathrm{H_2O}]$ is small and therefore the denominator is close to 1 and the quadratic term in the numerator is close to zero. Therefore, equation (3.6) becomes

$$k_{obs} = k_{3.1} + k_{3.3}K[\mathrm{H_2O}] \tag{3.7}$$

This assumption agrees with the experimental data in Cline et al.[1] that shows that the relationship between $[\mathrm{H_2O}]$ and k_{obs} is linear. Using the experimental data and a computational approximation for K, we can determine the rate constant for reaction (3.3).

3.1 *ab initio* calculations

Using Gaussian 03,[77] the geometries, anharmonic and harmonic vibrational frequencies, and rotational constants of both the β-HEP molecule and the β-HEP·$\mathrm{H_2O}$ complex were optimized with the B3LYP/aug-cc-pVDZ method and basis set. The energies were refined by performing single point energy calculations with the MP2 and CCSD(T) methods. All local minima geometries with energies within kT of the global minimum geometry at room temperature can be populated at room temperature and therefore were used in the equilibrium constant calculation. One global minimum and one local minimum structure were identified for the β-HEP molecule. These structures are shown in Figure 3.1. For the β-HEP $\cdot$ $\mathrm{H_2O}$ complex, a global minimum and 2 local minima structures were identified by random constrained sampling (RCS) methodology (see Figure 3.2). The RCS method generates β-HEP·$\mathrm{H_2O}$ geometries by randomly orienting a previously optimized water molecule within a constrained 3.0 angstrom radius sphere encompassing the optimized β-HEP structure. Seven hundred initial random geometries were used to establish the global and local minima. The energies

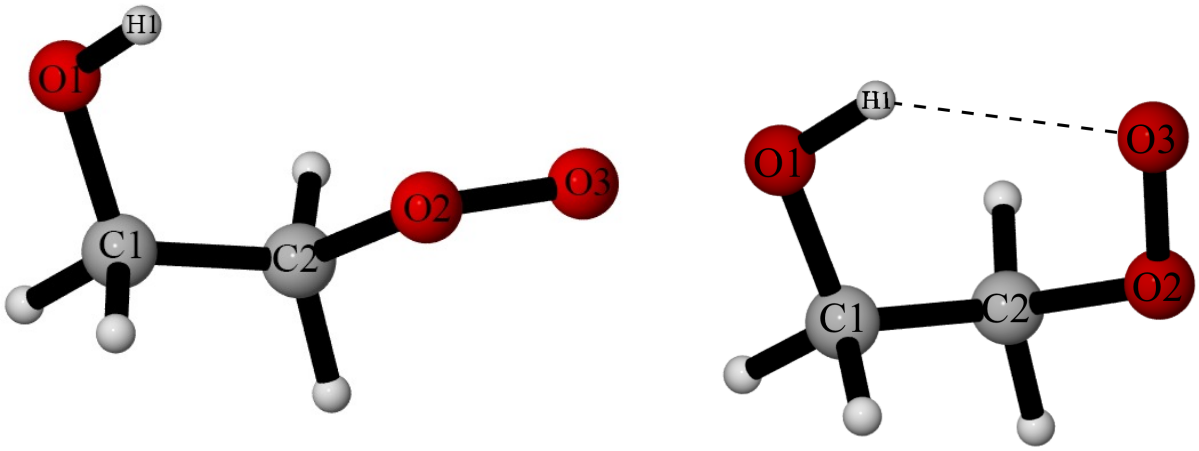

1 2

Figure 3.1: Optimized geometries of β-HEP.

of each structure were zero-point energy corrected and basis set superposition error corrected with the energies calculated with the B3LYP/aug-cc-pVDZ method and basis set.

3.2 Partition function calculations

Using the Gaussian calculations, the partition function of each geometry for each molecule was calculated according to the theory of McQuarrie et al.[78] and Steinfeld et al.[79] The overall partition function for a molecule is the product of the translational, rotational, electronic, and vibrational partition functions.

3.2.1 Translational, rotational, and electronic partition functions

The expressions for the translational (q^T), rotational (q^R), and electronic (q^E) partition functions are:

$$q^T = \frac{V\left(2\pi mkT\right)^{3/2}}{h^3} \tag{3.8}$$

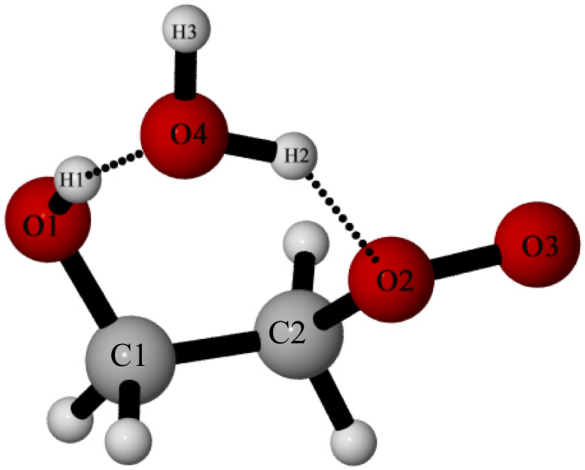

1

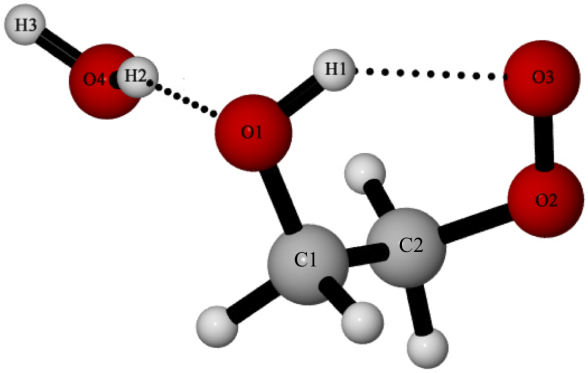

2

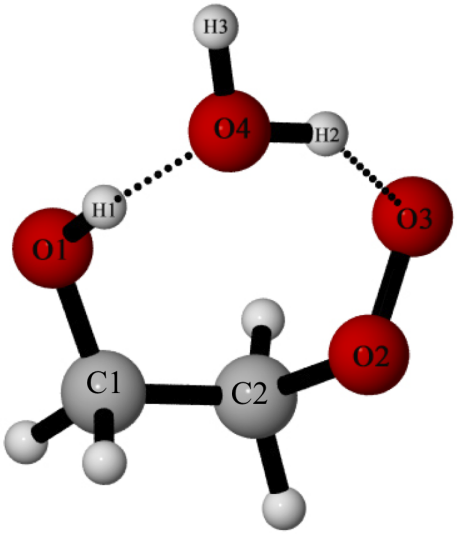

3

Figure 3.2: Optimized geometries of the β-HEP·H_2O complex.

where V is the volume of the reaction cell, m is the mass of the molecule, k is Boltzmann's constant, h is Planck's constant, and T is temperature;

$$q^R = \left(\frac{kT}{hc}\right)^{3/2} \left(\frac{\pi}{ABC}\right)^{1/2} \tag{3.9}$$

where c is the speed of light and A, B, and C are the rotational constants of the molecule;

$$q^E = ge^{-E/(RT)} \tag{3.10}$$

where g is the degeneracy of electronic ground states and E is the energy of the molecule. The energy in the partition function for all molecules and geometries must be in reference to the same zero-point energy.

3.2.2 Vibrational partition function

Assuming the normal vibrational modes of the molecule are independent, the vibrational partition function for a molecule is the product of the partition functions for each of its vibrational modes. The partition function of a vibrational mode can be calculated as the sum of the contributions from each vibrational state,

$$q^V = \sum_v e^{-\beta E_v} \tag{3.11}$$

where $\beta = 1/(kT)$. The energies of the vibrational states can be calculated according to several models for the vibrational motions. In this calculation, the harmonic oscillator, Morse oscillator, and hindered rotor models were used for each mode according to the model that best approximated the vibrational motion of the mode.

Harmonic oscillator

A harmonic approximation assumes that the energy levels of a vibrational mode are equally spaced. This approximation is accurate for the lowest vibrational states of most modes. Therefore the harmonic oscillator can be used for the highest vibrational frequencies, when only the ground and first excited states are populated. For a harmonic oscillator, equation (3.11) becomes

$$q^V = \sum_v e^{-\beta v h c \tilde{\nu}} = \frac{1}{1 - e^{-\beta h c \tilde{\nu}}} \tag{3.12}$$

where $\tilde{\nu}$ is the fundamental frequency of the vibrational mode. In this calculation, the fundamental anharmonic frequency calculated in Gaussian was used for $\tilde{\nu}$.

Morse oscillator

A Morse oscillator can be used to model vibrational modes that are dissociative. A harmonic oscillator model assumes that all vibrational states are equally spaced and does not account for the possibility that a bond can dissociate with sufficient energy. Therefore, the partition function based on the harmonic oscillator tends to underestimate the true partition function of the mode. The Morse oscillator accounts for the decreasing spacing between the vibrationally excited states and eventually the bond dissociation.

The energy levels for the Morse oscillator potential are defined by,

$$G(v) = \nu_e \left(v + \frac{1}{2} \right) + x_e \left(v + \frac{1}{2} \right)^2 \tag{3.13}$$

where ν_e is the fundamental harmonic vibrational frequency, v is the vibrational quantum number, and x_e is the diagonal element of the X-matrix corresponding to the vibrational mode. The X-matrix is a triangular matrix containing the anharmonic constants for each vibrational mode. The off-diagonal entries can be ignored if the vibrational modes are assumed to be independent. If x_e is negative, the bond will eventually dissociate, whereas if x_e is positive there are infinitely many bound states. For modes where x_e is positive, the

harmonic oscillator is used to calculate the partition function. The bond will dissociate when $G(v)$ achieves a maximum, or at $v^* = -\frac{\nu_e}{2x_e} - \frac{1}{2}$. Therefore, at the highest energy bound state, $v_{max} = \lfloor v^* \rfloor$, there are $N = v_{max} + 1$ bound states. The value for x_e is then adjusted based on this value,

$$\tilde{x_e} = -\frac{\nu_e}{2N} \tag{3.14}$$

For some states, if the vibration primarily involved the stretching of a hydrogen bond, $\tilde{x_e}$ was calculated from the dissociation energy for the breaking of the hydrogen bond, D,

$$\tilde{x_e} = -\frac{\nu_e^2}{4D} \tag{3.15}$$

N was then calculated as $-\frac{\nu_e}{2\tilde{x_e}}$ and rounded to the nearest integer. The partition function was then calculated,

$$q^V = \sum_{v=0}^{v_{max}} e^{-hc(G(v)-G(0)/(kT)} \tag{3.16}$$

using $\tilde{x_e}$ to calculate $G(v)$ and $G(0)$.

Hindered rotor

A hindered rotor model was used to model vibrations that involve the rotation of a functional group on the molecule. The calculation of the partition function for a hindered rotor vibration was based on McClurg et al.[80]

$$q^V = q_{HO} \left(\frac{r\pi}{\theta}\right)^{1/2} e^{-r/(2\theta)} I_0 \left(\frac{r}{2\theta}\right) \tag{3.17}$$

were q_{HO} is the partition function calculated as a harmonic oscillator using the fundamental harmonic frequency , and r and θ are defined as

$$r = \frac{\sqrt{2Iw}}{\hbar} \tag{3.18}$$

$$\theta = \frac{kT}{\hbar}\sqrt{\frac{2I}{w}} \tag{3.19}$$

where w is the barrier height for the hindered rotor (for this complex, the strength of one or two hydrogen bonds) and I is the moment of inertia for the rotation.

3.3 Local minima weighting

Three local minimum geometries for the complex and two local minimum geometries for β-HEP are all accessible at room temperature. Therefore the partition function for each of these geometries will contribute to the overall equilibrium constant for complex formation. The partition function for a molecule is equal to

$$q = \sum_i e^{-E_i/(kT)} \tag{3.20}$$

where i denotes each of the states for the molecule. Therefore the partition functions for β-HEP·H_2O and β-HEP are equal to the sums of the partition functions for each of the local minimum geometries. Therefore, the equilibrium constant for complex formation is equal to

$$K = \frac{\mathrm{q}_{[\mathrm{HEP-H2O}]_1} + \mathrm{q}_{[\mathrm{HEP-H2O}]_2} + \mathrm{q}_{[\mathrm{HEP-H2O}]_3}}{\left(\mathrm{q}_{[\mathrm{HEP}]_1} + \mathrm{q}_{[\mathrm{HEP}]_2}\right)\left(\frac{\mathrm{q}_{[\mathrm{H2O}]}}{V}\right)} \tag{3.21}$$

3.4 Results

The MATLAB code used for these calculations is given in the Appendix (see Appendix C). The model used to calculate the partition function for each vibrational mode is given in Tables 3.1, 3.2, 3.3, 3.4, and 3.5. The equilibrium constants for the experimental temperatures in Cline et al.[1] are given in Table 3.6 as well as the percent of β-HEP radicals that are complexed at each of the experimental water vapor concentrations. Table 3.7 gives the same results with the equilibrium constants calculated using only the harmonic oscillator model

with the calculated anharmonic frequencies. Based on the equilibrium constants in Table 3.6, the change in enthalpy for the complex formation is -2.51 kcal/mol and the change in entropy for the complex formation is -11.5 cal/mol. Based on the equilibrium constants in Table 3.7, the change in enthalpy for the complex formation is -2.57 kcal/mol and the change in entropy for the complex formation is 11.2 cal/mol.

The equilibrium constants calculated in this work are approximately two orders of magnitude smaller than the equilibrium constant for the formation of the $HO_2 \cdot H_2O$ complex ($(5.2 \pm 3.2) \times 10^{-19}$ cm^3 molecules^{-1} at 297 K)[66]. Further, the rate constant for reaction (3.3) at 296 K is calculated to be about 42 times greater than the rate constant for the reaction of HO_2 with its complex,

$$HO_2 \cdot H_2O + HO_2 \longrightarrow \text{Products} \tag{3.22}$$

The calculated rate constants for reaction (3.3) are unrealistically large, suggesting that the calculated equilibrium constants are underestimating the true values. It is expected that the calculated energies of β-HEP and the β-HEP$\cdot H_2O$ complex are biggest sources of error in the equilibrium constant calculation given that there is an exponential relationship between these energies and the calculated value for K.

Table 3.1: Descriptions and model assignments for each vibrational mode of the β-HEP geometry 1.

Vibrational energies (cm^{-1})			
Harmonic	**Anharmonic**	**Description**	**Model**
3808.454	3620.731	O1-H1 stretch	Morse oscillator
3138.67	2978.489	H-C2-H asymmetric stretch, slight H-C1-H asymmetric stretch	Morse oscillator
3102.507	2942.753	H-C1-H asymmetric stretch, slight H-C2-H symmetric stretch	Morse oscillator
3063.389	2945.038	H-C2-H symmetric stretch, slight H-C1-H asymmetric stretch	Morse oscillator
3020.096	2920.592	H-C1-H symmetric stretch, slight H-C2-H asymmetric stretch	Morse oscillator
1467.175	1442.891	H-C1-H bend	Harmonic oscillator
1453.278	1426.955	H-C2-H bend	Harmonic oscillator
1406.426	1368.388	C1-C2 stretch, C1 wag, C1-O1-H10 bend, slight C2 wag	Morse oscillator
1371.069	1335.751	C1-O1-H10 bend, C1 twist, C2 twist	Harmonic oscillator
1348.208	1322.522	C1 wag, C2 wag	Harmonic oscillator
1232.105	1202.985	C1 twist, C2 twist, C1-O1-H1 bend	Harmonic oscillator
1213.101	1184	C2 twist, C1 twist, C1-O1-H1 bend, O2-O3 stretch	Morse oscillator
1188.446	1163.568	O2-O3 stretch, C2 rock, C1-O1-H1 bend	Morse oscillator

Continued on next page

Table 3.1 – continued from previous page

Vibrational energies (cm^{-1})			
Harmonic	**Anharmonic**	**Description**	**Model**
1091.95	1060.685	asymmetric C1-C2-O2 stretch, O1-C1 stretch, C2 rock, C1 rock	Morse oscillator
1083.61	1056.915	asymmetric C2-C1-O1 stretch, C1 rock, C1-O1-H1 bend	Morse oscillator
994.399	964.177	asymmetric C1-C2-O2 stretch, C1 rock, C1-O1-H1 bend	Morse oscillator
881.159	863.91	symmetric C2-C1-O1 stretch, C2 twist, C1 wag	Morse oscillator
807.606	786.947	C2-O2 stretch, C1 twist	Morse oscillator
543.74	538.518	C2-O2-O3 bend, C2-C1-O1 bend, C1-C2-O2 bend	Harmonic oscillator
404.076	401.323	C2-O2-O3 bend, C2-C1-O1 bend	Harmonic oscillator
346.292	289.348	O1-H1 rotation (internal hydrogen bond stretch)	Hindered rotor
264.723	260.804	C2-C1-O1-H1 torsion (internal hydrogen bond stretch)	Harmonic oscillator
141.507	133.697	O2-C2-C1-O1 torsion (internal hydrogen bond stretch)	Morse oscillator (D = 1 H bond)
54.863	48.725	C1-C2-O2-O3 torsion	Hindered rotor

Table 3.2: Descriptions and model assignments for each vibrational mode of the β-HEP geometry 2.

Vibrational energies (cm^{-1})			
Harmonic	**Anharmonic**	**Description**	**Model**
3752.783	3550.24	O1-H1 stretch (internal H-bond stretch)	Morse oscillator
3141.553	2980.548	C2 asymmetric stretch, slight C1 symmetric stretch	Morse oscillator
3086.371	2929.97	C1 asymmetric stretch, C2 symmetric stretch	Morse oscillator
3070.189	2928.563	C2 symmetric stretch, C1 asymmetric stretch	Morse oscillator
3004.13	2851.047	C1 symmetric stretch	Morse oscillator
1469.864	1449.33	H-C1-H bend	Harmonic oscillator
1445.871	1407.805	H-C2-H bend, slight C1-O1-H1 bend	Harmonic oscillator
1424.181	1386.483	C1-O1-H1 bend, C1 wag, H-C2-H bend	Harmonic oscillator
1363.81	1334.697	C1 twist, C1-O1-H1 bend, C2 wag, C1-C2 stretch	Morse oscillator
1349.184	1323.463	C2 rock, C1 twist, C1-O1-H1 bend, O2-O3 stretch	Morse oscillator
1264.498	1241.179	C1 twist, C2 twist, C1-O1-H1 bend, O2-O3 stretch	Morse oscillator
1212.283	1188.72	C1 twist, C2 twist, C1-O1-H1 bend	Morse oscillator
1165.923	1138.878	C2-O2-O3 asymmetric stretch, C2 twist, C1-O1-H1 bend, C1 wag	Morse oscillator

Continued on next page

Table 3.2 – continued from previous page

Vibrational energies (cm^{-1})			
Harmonic	**Anharmonic**	**Description**	**Model**
1106.503	1076.863	C2-O2-O3 asymmetric stretch, C1-O1 stretch, C2 rock	Morse oscillator
1080.08	1051.029	C2-C1-O1 asymmetric stretch, C1-O1-H1 bend	Morse oscillator
960.85	943.104	C1-C2-O2 asymmetric stretch, C1-O1-H1 bend	Morse oscillator
919.905	897.514	C2-C1-O1 symmetric stretch, O2-C2 stretch, C2 twist, C1 rock	Morse oscillator
795.951	772.468	C1-C2-O2 symmetric stretch, C1 rock, C2 rock	Morse oscillator
549.727	546.89	C1 rock, C2 rock, C2-O2-O3 bend	Harmonic oscillator
458.296	406.997	O1-H rotation	Hindered rotor
398.368	386.08	C2-O2-O3 bend, C2-C1-O1 bend	Harmonic oscillator
329.394	331.744	O2-C2-C1-O1 torsion	Harmonic oscillator
167.325	155.733	O2-C2-C1-O1 torsion (internal H-bond stretch)	Morse oscillator (D = 1 H bond)
85.73	76.251	O3-O2-C2-C1 torsion	Hindered rotor

Table 3.3: Descriptions and model assignments for each vibrational mode of the β-HEP·H_2O geometry 1.

Vibrational energies (cm^{-1})			
Harmonic	**Anharmonic**	**Description**	**Model**
3884.624	3710.42	asymmetric H-O4-H stretch	Morse oscillator
3763.657	3602.542	symmetric H-O4-H stretch, slight O1-H1 stretch	Morse oscillator
3623.795	3450.074	O1-H1 stretch, slight symmetric H-O4-H stretch	Morse oscillator
3140.683	2978.545	asymmetric H-C2-H stretch	Morse oscillator
3080.176	2925.162	asymmetric H-C1-H stretch, slight symmetric H-C2-H stretch	Morse oscillator
3064.985	2921.268	symmetric H-C2-H stretch, slight asymmetric H-C1-H stretch	Morse oscillator
3012.56	2877.319	symmetric H-C1-H stretch	Morse oscillator
1610.99	1564.458	H-O4-H bend	Harmonic oscillator
1461.722	1424.518	H-C1-H bend, C1-O1-H1 bend, slight H-C2-H bend	Harmonic oscillator
1458.609	1418.46	C1-O1-H1 bend, H-C1-H bend, H-C2-H bend	Harmonic oscillator
1445.825	1407.479	H-C2-H bend, C1-O1-H1 bend, slight H-C1-H bend	Harmonic oscillator
1390.41	1368.519	C1 rock, slight C2 rock	Harmonic oscillator
1351.387	1328.475	C2 rock, slight C1 rock	Harmonic oscillator

Continued on next page

Table 3.3 – continued from previous page

Vibrational energies (cm^{-1})			
Harmonic	**Anharmonic**	**Description**	**Model**
1267.043	1234.442	C1-O1-H1 bend, C1 twist, C2 twist	Harmonic oscillator
1211.189	1188.518	C2 twist, C1 twist, O2-O3 stretch	Morse oscillator
1194.849	1169.033	O2-O3 stretch, C2 twist, C1 twist, C1-O1-H1 bend	Morse oscillator
1105.384	1074.655	asymmetric O1-C1-C2 stretch	Morse oscillator
1085.61	1065.62	C1-C2 stretch, C1 rock, C2 rock, O1-H1 rock	Morse oscillator
1000.808	967.823	asymmetric C1-C2-O2 stretch	Morse oscillator
882.419	864.028	symmetric O1-C1-C2 stretch	Morse oscillator
801.216	785.003	C2-O2 stretch, C1 rock	Morse oscillator
657.191	519.674	O1-H1 twist, O4-H2 wag	Hindered rotor
537.95	535.28	C2-O2-O3 bend, C2-C1-O1 bend	Harmonic oscillator
396.595	394.653	C2-O2-O3 bend, C2-C1-O1 bend, O2-H2 hydrogen bond stretch	Harmonic oscillator
367.807	294.704	Water rock, O1-H1 twist	Hindered rotor
287.248	274.835	Water rock, C1-C2-O2 bend	Hindered rotor
269.167	282.902	Water rock, C1-C2-O2 bend	Hindered rotor

Continued on next page

Table 3.3 – continued from previous page

Vibrational energies (cm^{-1})			
Harmonic	**Anharmonic**	**Description**	**Model**
195.477	180.76	O9-H1-O4 hydrogen bond stretch, C1 rock, C2 rock	Morse oscillator (D = 1 H bond)
171.697	206.513	Water rock	Hindered rotor
134.144	131.717	C1-C2-O2-O3 torsion, O4-H1 and O2-H2 hydrogen bond stretch	Morse oscillator (D = 2 H bonds)
100.797	100.423	O2-H2 hydrogen bond stretch	Morse oscillator (D = 1 H bond)
58.803	79.038	C1-C2-O2-O3 torsion, O4-H3 wag	Hindered rotor
54.437	74.147	C1-C2-O2-O3 torsion, H3 twist	Hindered rotor

Table 3.4: Descriptions and model assignments for each vibrational mode of the β-HEP·H_2O geometry 2.

Vibrational energies (cm^{-1})			
Harmonic	**Anharmonic**	**Description**	**Model**
3877.979	3682.346	H-O4-H asymmetric stretch	Morse oscillator
3722.461	3513.514	O1-H1 stretch	Morse oscillator
3630.932	3466.145	H-O4-H symmetric stretch	Morse oscillator
3147.833	2986.742	H-C2-H asymmetric stretch	Morse oscillator
3108.528	2945.878	H-C1-H asymmetric stretch, slight H-C2-H stretch	Morse oscillator
3078.215	2936.813	H-C2-H symmetric stretch, C1-H stretch	Morse oscillator
3029.396	2920.194	H-C1-H symmetric stretch	Morse oscillator
1638.86	1578.284	H-O4-H bend	Harmonic oscillator
1470.694	1438.092	H-C1-H bend	Harmonic oscillator
1453.946	1413.993	H-C2-H bend, slight C1-O1-H1 bend	Harmonic oscillator
1429.695	1393.897	C1-O1-H1 bend, C1 wag, slight H-C2-H bend	Harmonic oscillator
1368.992	1340.39	C1 wag, C2 wag, C1-O1-H1 bend	Harmonic oscillator
1350.039	1316.84	C2 wag, C1 wag, C1-O1-H1 bend	Harmonic oscillator

Continued on next page

Table 3.4 – continued from previous page

Vibrational energies (cm^{-1})			
Harmonic	**Anharmonic**	**Description**	**Model**
1264.195	1243.681	C2 wag, C1 rock, C1-O1-H1 bend, slight O2-O3 stretch	Harmonic oscillator
1213.274	1186.891	C1 twist, C1-O1-H1 bend, C2 wag	Harmonic oscillator
1170.104	1141.487	asymmetric O3-O2-C2 stretch, C2 twist, C1 rock	Morse oscillator
1092.289	1063.643	C1-O1 stretch, C2 rock	Morse oscillator
1078.947	1047.332	O1-C1-C2 asymmetric stretch, O1-H1 bend	Morse oscillator
963.924	934.928	C1-C2-O2 asymmetric stretch, O1-H1 bend	Morse oscillator
918.278	893.996	O1-C1-C2 symmetric stretch, C2-O2 stretch, C2 twist	Morse oscillator
796.967	770.532	C1-C2-O2 symmetric stretch	Morse oscillator
656.142	553.139	O1-H1 rotation, O4-H2 rotation	Hindered rotor
560.58	557.104	C2-O2-O3 bend, C1 rock	Harmonic oscillator
497.41	439.033	O1-H1 rotation, O4-H2 rotation	Hindered rotor
404.139	382.336	O1-C1-C2 bend, C2-O2-O3 bend, water rotation, O4-H2-O1 hydrogen bond stretch)	Harmonic oscillator
387.258	332.271	Water rotation	Hindered rotor
329.371	326.749	O1-C1-C2-O2 torsion, water rock	Harmonic oscillator

Continued on next page

Table 3.4 – continued from previous page

Vibrational energies (cm^{-1})			
Harmonic	**Anharmonic**	**Description**	**Model**
207.587	178.212	O1-H1 twist, C1 wag, O1-H2 hydrogen bond stretch	Morse oscillator (D = 1 H bond)
161.221	137.193	C1-C2-O2-O3 torsion, water H3 rotation	Morse oscillator (D = 1 H bond)
142.246	29.604	O4-H3 rotation	Hindered rotor
95.783	83.817	C1-C2-O2-O3 torsion, water rock	Hindered rotor
70.17	64.337	Water rock, C1-C2-O2-O3 torsion	Morse oscillator
38.758	42.589	Water rotation	Morse oscillator (D = 1 H bond)

Table 3.5: Descriptions and model assignments for each vibrational mode of the β-HEP·H_2O geometry 3.

Vibrational energies (cm^{-1})			
Harmonic	**Anharmonic**	**Description**	**Model**
3871.709	3686.083	H-O4-H asymmetric stretch	Morse oscillator
3714.928	3552.778	H-O4-H symmetric stretch, slight O1-H1 stretch	Morse oscillator
3584.086	3409.18	O1-H1 stretch	Morse oscillator
3154.358	2990.939	H-C4-H asymmetric stretch	Morse oscillator
3074.735	2917.101	H-C1-H asymmetric stretch, H-C4-H symmetric stretch	Morse oscillator
3064.241	2913.621	H-C1-H asymmetric stretch, H-C4-H symmetric stretch	Morse oscillator
3010.526	2911.606	symmetric H-C1-H stretch	Morse oscillator
1623.448	1565.338	H-O4-H bend	Harmonic oscillator
1462.821	1437.314	H-C1-H bend	Harmonic oscillator
1454.934	1402.555	C1-O1-H bend, H-C4-H bend, C1 twist	Harmonic oscillator
1433.506	1398.469	H-C4-H bend, slight C1-O1-H1 bend	Harmonic oscillator
1382.009	1343.476	C1 wag, slight C4 twist	Harmonic oscillator
1340.161	1313.445	C4 wag, slight C1 twist	Harmonic oscillator

Continued on next page

Table 3.5 – continued from previous page

Vibrational energies (cm^{-1})			
Harmonic	**Anharmonic**	**Description**	**Model**
1276.861	1243.981	C4 twist, O2-O3 stretch, slight C1-O1-H1 bend, slight C1 twist	Morse oscillator
1243.548	1209.01	C1 twist, C1-O1-H1 bend, slight C4 twist	Harmonic oscillator
1171.687	1145.182	O2-O3 stretch, C4 twist, C1-O1 stretch	Morse oscillator
1111.839	1081.486	C1-O1 stretch,C4-O2-O3 asymmetric stretch	Morse oscillator
1085.409	1054.537	C4-C1-O1 asymmetric stretch, C1-O1-H1 bend	Morse oscillator
960.068	934.421	O2-C4-C1 asymmetric stretch	Morse oscillator
887.904	869.625	O1-C1-C4 symmetric stetch, C4-C7 stretch	Morse oscillator
806.084	779.558	C1-C4-O2 symmetric stretch	Morse oscillator
705.927	628.456	C1-O1-H1 rotation, O4-H2 rotation	Hindered rotor
504.673	492.383	C4-O2-O3 bend, C4 rock	Harmonic oscillator
479.451	468.157	O3-O2-C4-C1 torsion, O1-C1-C4 bend, water wag	Harmonic oscillator
417.565	323.716	C1-O1-H1 rotation, O4-H2 rotation	Hindered rotor
331.227	262.393	H-O4-H (water) rotation	Hindered rotor
308.617	305.005	C1-C4-O2-O3 torsion	Harmonic oscillator
226.614	33.755	O4-H3 rotation	Hindered rotor

Continued on next page

Table 3.5 – continued from previous page

Vibrational energies (cm^{-1})			
Harmonic	**Anharmonic**	**Description**	**Model**
189.776	151.106	O1-H1-O4 hydrogen bond stretch, O4-H rotation, C1 wag	Morse oscillator (D = 1 H bond)
144.033	111.388	O4-H2-O3 hydrogen bond stretch, O2-O3 rotation, O2-C4-C1-O1 torsion	Morse oscillator (D = 1 H bond)
117.766	108.927	asymmetric hydrogen bond stretch, O2-C4-C1-O1 torsion	Morse oscillator (D = 2 H bonds)
92.24	62.104	O2-O3 rotation, O4-H3 rotation	Hindered rotor
67.873	38.172	O3-O2-C4-C1 torsion, O4-H3 rotation	Harmonic oscillator

Table 3.6: Calculated values for the equilibrium constant, $k_{3.3}$, and percent of β-HEP complexed using the models assigned to each vibrational mode in Tables 3.1, 3.2, 3.3, 3.4, and 3.5 to calculate the vibrational partition function. Values for $Kk_{3.3}$ and temperatures and water vapors shown are taken from the experimental work done by Cline et al.[1]

Temperature	**K (cm^3 $molecules^{-1}$)**	**$Kk_{3.3}$**	**$k_{3.3}$ (cm^3 $molecules^{-1}$ s^{-1})**	**$[H_2O]$/1E16**	**% complexed**
274 K	9.3E-21	7.3E-29	7.9E-09	0.18	1.67E-03
				1.57	1.46E-02
				2.60	2.41E-02
				3.32	3.08E-02
280 K	7.6E-21	2.9E-29	3.8E-09	0.29	2.19E-03
				2.10	1.59E-02
				4.70	3.55E-02
				5.86	4.43E-02
				6.76	5.11E-02
288 K	5.8E-21	1.2E-29	2.1E-09	0.20	1.17E-03
				3.80	2.22E-02
				8.21	4.79E-02
				12.20	7.11E-02
296 K	4.6E-21	2.9E-30	0.63E-09	0.18	8.23E-04
				6.26	2.86E-02
				11.80	5.40E-02
				22.50	1.03E-01

Table 3.7: Calculated values for the equilibrium constant, $k_{3.3}$, and percent of β-HEP complexed using the harmonic oscillator model for all vibrational modes to calculate the vibrational partition function. Values for $Kk_{3.3}$ and temperatures and water vapors shown are taken from the experimental work done by Cline et al.[1]

Temperature	**K (cm^3 $molecules^{-1}$)**	**$Kk_{3.3}$**	**$k_{3.3}$ (cm^3 $molecules^{-1}$ s^{-1})**	**$[H_2O]$/1E16**	**% complexed**
274 K	1.7E-20	7.3E-29	4.3E-09	0.18	3.1E-03
				1.57	2.7E-02
				2.60	4.4E-02
				3.32	5.7E-02
280 K	1.4E-20	2.9E-29	2.1E-09	0.29	4.0E-03
				2.10	2.9E-02
				4.70	6.5E-02
				5.86	8.1E-02
				6.76	9.3E-02
288 K	1.1E-20	1.2E-29	1.1E-09	0.20	2.1E-03
				3.80	4.0E-02
				8.21	8.7E-02
				12.20	1.3E-01
296 K	8.2E-21	2.9E-30	0.35E-09	0.18	1.5E-03
				6.26	5.1E-02
				11.80	9.7E-02
				22.50	1.8E-01

Chapter 4

Conclusions and future work

As regions across the United States strive to achieve the National Ambient Air Quality Standards (NAAQS), policy makers depend on atmospheric modeling to understand the effects of various anthropogenic emissions. However these models are incomplete. Particularly, the effect of biogenic VOCs on the production of tropospheric ozone has traditionally been underestimated or unaccounted for. In 1988, Chemeides et al.[81] showed that in urban areas such as Atlanta, GA, if the biogenic VOC concentration was high enough (50 kg km^{-2}, their estimate for daytime biogenic VOC emissions), the complete elimination of anthropogenic VOC emissions would not be sufficient to achieve the NAAQS for ozone. Therefore, reductions in both NO_x and VOC emissions were necessary to achieve the standard. Accurate models for the effects of biogenic emissions generate accurate ozone isopleths, facilitating realistic and effective plans for improving air quality.

Desert climates are typically assumed to have low VOC/NO_x ratios.[47] However, in Tucson the "weekday effect," typical of areas with high VOC/NO_x ratios, was observed during the monsoon months though the "weekend effect" (typical of low VOC/NO_x ratios) was observed during more arid seasons. Diem[47] explained this shift by accounting for the increased emission of biogenic VOCs during the monsoon season. With better characterizations of desert shrub emissions and their reactions in the troposphere, the atmospheric chemistry in desert climates can be better understood and more accurately modeled.

In order to include the rate constant for thujone + $Cl^{\cdot}$ in atmospheric models, the emission rate and tropospheric concentration of thujone must be measured. Although thujone

has been identified as a major emission from some plants,[46,49] the emission rate has not been quantified. Some other VOCs characteristic of desert plants include artemiseole, artemisia alcohol, α-terpineol, and homosalate. The kinetics of the reactions of these molecules with $OH^{\cdot}$ and $Cl^{\cdot}$ have not yet been measured. The secondary chemistry that occurs after these VOCs are oxidized, including the formation and reaction of peroxy radicals with each other and NO, also needs to be studied to accurately account for these molecules in atmospheric models.

Thujone is emitted by Great Basin sagebrush which is commonly found in dessert regions and therefore will not often be exposed to high water vapor concentrations. However, during seasons of high humidity and precipitation (i.e. monsoon seasons) water vapor may play a role in catalyzing the reaction kinetics of the peroxy radical formed from thujone. Such seasons are often accompanied by high VOC emissions,[47] suggesting that water may in fact play a significant factor in the reaction kinetics of the peroxy radical formed from thujone. In shrub-dominated lands, atmospheric water vapor concentrations can also rise when snow is on the ground during the winter. Winter is also the time when shrubs experience the most herbivore damage, inducing increased VOC emissions. Therefore, with increased concentrations of thujone emitted and higher water vapor concentrations and lower temperatures, winter may be another time when the role of water vapor on the self-reaction of the peroxy radical from thujone is important.

The work presented here for the calculation of the equilibrium constant for the formation of the β-HEP$\cdot H_2O$ complex lends insight into the role of water vapor in the observed rate enhancement of peroxy radical reactions. The equilibrium constant for formation of the β-HEP$\cdot H_2O$ complex is larger at colder temperatures but decreases quickly as the temperature is raised. Even though the equilibrium constant is smaller at warmer temperatures, more complex is formed at warmer temperatures because a larger concentration of water vapor can exist in warm air compared to colder air (see Table 3.6). Therefore, the larger enhancement that is observed at colder temperatures is attributed to the strong temperature dependence

in $k_{3.3}$ and not to the amount of complex that exists under these conditions. This conclusion is further supported by the values for $k_{3.3}$ in Tables 3.6 and 3.7. These values show a strong, negative temperature dependence, characteristic of radical reactions. In radical self reactions, the radicals associate and require a third body to collide and carry away energy in order to form the pre-reactive complex, which is at lower energy than the reactants. It is expected that water catalyzes this reaction by providing a mechanism for energy removal from the associated radicals, therefore speeding the formation of the pre-reactive complex. The results presented here are preliminary and therefore the values for $k_{3.3}$ in Tables 3.6 and 3.7 may not be accurate. Nevertheless we expect that the trends described here reflect the true trends.

To better understand the role water vapor plays on the reactivity of β-HEP, the reactions of β-HEP with $HO_2^{\cdot}$ and NO in the presence of water should be measured. These kinetic studies will also contribute to a complete model of the reaction pathway of β-HEP and understanding its role in the chemistry of the troposphere.

Improper analysis of peroxy radical reactions will continue unless a general understanding of water catalysis in the troposphere is refined. The absence of self-reaction enhancement by water in current atmospheric pollution models leads to prediction of more β-HEP in the troposphere than is measured. A clear understanding of this water vapor catalysis mechanism will become increasingly more important as climate change leads to increasing water vapor concentrations.

References

[1] Cline, T. S.; Kumbhani, S.; Clark, J.; Killian, M. C.; Shirts, R.; Hansen, L. E.; Hansen, J. C. Water vapor enhancement of the $HO_2CH_2CH_2O_2$ self-reaction rate. *in preparation*

[2] EPA, What Are the Six Common Air Pollutants? 2012; `http://www.epa.gov/airquality/urbanair/`.

[3] EPA, State Implementation Plan Development Process. 2012; `http://www.epa.gov/air/urbanair/sipstatus/process.html`.

[4] Schlink, U.; Herbarth, O.; Richter, M.; Dorling, S.; Nunnari, G.; Cawley, G.; Pelikan, E. Statistical models to assess the health effects and to forecast ground-level ozone. *Environmental Modelling and Software* **2006**, *21*, 547–558.

[5] Mudway, I.; Kelly, F. Ozone and the lung: a sensitive issue. *Molecular Aspects of Medicine* **2000**, *21*, 1–48.

[6] EPA, Health Effects of Ozone in the General Population. 2012; `http://www.epa.gov/apti/ozonehealth/population.html`.

[7] Fraga, J.; Botelho, A.; Sa, A.; Costa, M.; Quaresma, M. The Lag Structure and the General Effect of Ozone Exposure on Pediatric Respiratory Morbidity. *International Journal of Environmental Research and Public Health* **2011**, *8*, 4013–4024.

[8] Bell, M.; McDermott, A.; Zeger, S.; Samet, J.; Dominici, F. Ozone and short-term mortality in 95 US urban communities, 1987-2000. *Journal of the American Medical Association* **2004**, *292*, 2372–2378.

[9] Ashmore, M. Assessing the future global impacts of ozone on vegetation. *Plant Cell and Environment* **2005**, *28*, 949–964.

[10] Miller, P. R.; DeBauer, M. D.; Nolasco, A. Q.; Tejeda, T. H. Comparison of Ozone Exposure Characteristics in Forested Regions Near Mexico City and Los Angeles. *Atmospheric Environment* **1994**, *28*, 141–148.

[11] Avnery, S.; Mauzerall, D. L.; Liu, J.; Horowitz, L. W. Global crop yield reductions due to surface ozone exposure: 1. Year 2000 crop production losses and economic damage. *Atmospheric Environment* **2011**, *45*, 2284–2296.

[12] Avnery, S.; Mauzerall, D. L.; Liu, J.; Horowitz, L. W. Global crop yield reductions due to surface ozone exposure: 2. Year 2030 potential crop production losses and economic damage under two scenarios of O-3 pollution. *Atmospheric Environment* **2011**, *45*, 2297–2309.

[13] Finlayson-Pitts, B. J.; Pitts, J. N. *Chemistry of the upper and lower atmosphere: theory, experiments, and applications*; Academic Press: San Diego, CA, USA, 2000; Chapter Particles in the Troposphere, pp 349–435.

[14] McDonald, J. D.; Doyle-Eisele, M.; Kracko, D.; Lund, A.; Surratt, J. D.; Hersey, S. P.; Seinfeld, J. H.; Rohr, A. C.; Knipping, E. M. Cardiopulmonary response to inhalation of secondary organic aerosol derived from gas-phase oxidation of toluene. *Inhalation toxicology* **2012**, *24*, 689–697.

[15] Brook, R. D.; Rajagopalan, S.; III, C. A. P.; Brook, J. R.; Bhatnagar, A.; Diez-Roux, A. V.; Holguin, F.; Hong, Y.; Luepker, R. V.; Mittleman, M. A.; Peters, A.; Siscovick, D.; Jr., S. C. S.; Whitsel, L.; Kaufman, J. D. Particulate Matter Air Pollution and Cardiovascular Disease An Update to the Scientific Statement From the American Heart Association. *Circulation* **2010**, *121*, 2331–2378.

[16] Forster, P.; Ramaswamy, V.; Artaxo, P.; Berntsen, T.; Betts, R.; Fahey, D. W.; Haywood, J.; Lean, J.; Lowe, D. C.; Myhre, G.; Nganga, J.; Prinn, R.; Raga, G.; Schulz, M.; Dorland, R. V. In *Changes in Atmospheric Constitutents and in Radiative Forcing*; Solomon, S., Qin, D., Manning, M., Chen, Z., Marquis, M., Averyt, K. B., Tignor, M., Miller, H. L., Eds.; Climate Change 2007: The Physical Science Basis. Contribution of Working Group I to the Fourth Assessment Report of the Intergovernmental Panel on Climate Change; Cambridge University Press: Cambridge, United Kingdom and New York, NY, USA, 2007.

[17] Guenther, A. et al. A Global-Model of Natural Volatile Organic-Compound Emissions. *Journal of Geophysical Research-Atmospheres* **1995**, *100*, 8873–8892.

[18] Atkinson, R.; Arey, J. Gas-phase tropospheric chemistry of biogenic volatile organic compounds: a review. *Atmospheric Environment* **2003**, *37*, S197–S219.

[19] Abelson, P. Rural and Urban Ozone. *Science* **1988**, *241*, 1569–1569.

[20] Fuentes, J.; Lerdau, M.; Atkinson, R.; Baldocchi, D.; Bottenheim, J.; Ciccioli, P.; Lamb, B.; Geron, C.; Gu, L.; Guenther, A.; Sharkey, T.; Stockwell, W. Biogenic hydrocarbons in the atmospheric boundary layer: A review. *Bulletin of the American Meteorological Society* **2000**, *81*, 1537–1575.

[21] Finlayson-Pitts, B. J.; Pitts, J. N. *Chemistry of the upper and lower atmosphere: theory, experiments, and applications*; Academic Press: San Diego, 2000.

[22] Atkinson, R. Atmospheric chemistry of VOCs and NOx. *Atmospheric Environment* **2000**, *34*, 2063–2101.

[23] Kumar, U.; Prakash, A.; Jain, V. K. A Multivariate Time Series Approach to Study the Interdependence among O3, NOx, and VOCs in Ambient Urban Atmosphere. *Environmental Modeling and Assessment* **2009**, *14*, 631–643.

[24] Finlayson-Pitts, B. J.; Pitts, J. N. *Chemistry of the upper and lower atmosphere: theory, experiments, and applications*; Academic Press: San Diego, CA, USA, 2000; Chapter Applications of Atmospheric Chemistry, pp 871–942.

[25] Finlayson-Pitts, B. J.; Pitts, J. N. Volatile Organic Compounds: Ozone Formation, Alternative Fuels and Toxics. *Chemistry and Industry* **1993**, 796–800.

[26] Sjostedt, S. J.; Slowik, J. G.; Brook, J. R.; Chang, R. Y. W.; Mihele, C.; Stroud, C. A.; Vlasenko, A.; Abbatt, J. P. D. Diurnally resolved particulate and VOC measurements at a rural site: indication of significant biogenic secondary organic aerosol formation. *Atmospheric Chemistry and Physics* **2011**, *11*, 5745–5760.

[27] Tsigaridis, K.; Kanakidou, M. Global modelling of secondary organic aerosol in the troposphere: a sensitivity analysis. *Atmospheric Chemistry and Physics* **2003**, *3*, 1849–1869.

[28] Hao, L. Q. et al. Mass yields of secondary organic aerosols from the oxidation of alpha-pinene and real plant emissions. *Atmospheric Chemistry and Physics* **2011**, *11*, 1367–1378.

[29] Mentel, T. F.; Wildt, J.; Kiendler-Scharr, A.; Kleist, E.; Tillmann, R.; Maso, M. D.; Fisseha, R.; Hohaus, T.; Spahn, H.; Uerlings, R.; Wegener, R.; Griffiths, P. T.; Dinar, E.; Rudich, Y.; Wahner, A. Photochemical production of aerosols from real plant emissions. *Atmospheric Chemistry and Physics* **2009**, *9*, 4387–4406.

[30] Yu, S.; Mathur, R.; Schere, K.; Kang, D.; Pleim, J.; Young, J.; Tong, D.; Pouliot, G.; McKeen, S. A.; Rao, S. T. Evaluation of real-time PM(2.5) forecasts and process analysis for PM(2.5) formation over the eastern United States using the Eta-CMAQ forecast model during the 2004 ICARTT study. *Journal of Geophysical Research-Atmospheres* **2008**, *113*, D06204.

[31] Carlton, A. G.; Wiedinmyer, C.; Kroll, J. H. A review of Secondary Organic Aerosol (SOA) formation from isoprene. *Atmospheric Chemistry and Physics* **2009**, *9*, 4987–5005.

[32] Lamb, B.; Westberg, H.; Allwine, G.; Quarles, T. Biogenic Hydrocarbon Emissions from Deciduous and Coniferous Trees in the United States. *Journal of Geophysical Research-Atmospheres* **1985**, *90*, 2380–2390.

[33] Lamb, B.; Gay, D.; Westberg, H.; Pierce, T. A Biogenic Hydrocarbon Emission Inventory for the USA using a Simple Forest Canopy Model. *Atmos.Environ.Part A* **1993**, *27*, 1673–1690.

[34] Reissell, A.; Arey, J. Biogenic volatile organic compounds at Azusa and elevated sites during the 1997 Southern California Ozone Study. *Journal of Geophysical Research-Atmospheres* **2001**, *106*, 1607–1621.

[35] Paulson, S.; Flagan, R.; Seinfeld, J. Atmospheric Photooxidation of Isoprene 1. the Hydroxyl Radical and Ground-State Atomic Oxygen Reactions. *International Journal of Chemical Kinetics* **1992**, *24*, 79–101.

[36] Paulson, S.; Flagan, R.; Seinfeld, J. Atmospheric Photooxidation of Isoprene 2. the Ozone-Isoprene Reaction. *International Journal of Chemical Kinetics* **1992**, *24*, 103–125, PT: J; UT: WOS:A1992GV66500009.

[37] Hoyle, C. R.; Berntsen, T.; Myhre, G.; Isaksen, I. S. A. Secondary organic aerosol in the global aerosol - chemical transport model Oslo CTM2. *Atmospheric Chemistry and Physics* **2007**, *7*, 5675–5694.

[38] Seinfeld, J. H. *Atmospheric chemistry and physics : from air pollution to climate change*, 2nd ed.; Wiley: Hoboken, N.J., c2006.

[39] Guenther, A.; Geron, C.; Pierce, T.; Lamb, B.; Harley, P.; Fall, R. Natural emissions of non-methane volatile organic compounds; carbon monoxide, and oxides of nitrogen from North America. *Atmos.Environ.* **2000**, *34*, 2205–2230.

[40] Geron, C.; Rasmussen, R.; Arnts, R.; Guenther, A. A review and synthesis of monoterpene speciation from forests in the United States. *Atmospheric Environment* **2000**, *34*, 1761–1781.

[41] von Hessberg, C.; von Hessberg, P.; Poeschl, U.; Bilde, M.; Nielsen, O. J.; Moortgat, G. K. Temperature and humidity dependence of secondary organic aerosol yield from the ozonolysis of beta-pinene. *Atmospheric Chemistry and Physics* **2009**, *9*, 3583–3599.

[42] Saathoff, H.; Naumann, K. H.; Moehler, O.; Jonsson, A. M.; Hallquist, M.; Kiendler-Scharr, A.; Mentel, T. F.; Tillmann, R.; Schurath, U. Temperature dependence of yields of secondary organic aerosols from the ozonolysis of alpha-pinene and limonene. *Atmospheric Chemistry and Physics* **2009**, *9*, 1551–1577.

[43] Corchnoy, S.; Atkinson, R. Kinetics of the Gas-Phase Reactions of OH and NO3 Radicals with 2-Carene, 1,8-Cineole, Para-Cymene, and Terpinolene. *Environmental science and technology* **1990**, *24*, 1497–1502.

[44] Chen, X.; Hopke, P. K. A chamber study of secondary organic aerosol formation by limonene ozonolysis. *Indoor air* **2010**, *20*, 320–328.

[45] Seinfeld, J.; Erdakos, G.; Asher, W.; Pankow, J. Modeling the formation of secondary organic aerosol (SOA). 2. The predicted effects of relative humidity on aerosol formation in the alpha-pinene-, beta-pinene-, sabinene-, Delta(3)-Carene-, and cyclohexene-ozone systems. *Environmental science and technology* **2001**, *35*, 1806–1817.

[46] Arey, J.; Crowley, D.; Crowley, M.; Resketo, M.; Lester, J. Hydrocarbon Emissions from Natural Vegetation in California South-Coast-Air-Basin. *Atmospheric Environment* **1995**, *29*, 2977–2988.

[47] Diem, J. Comparisons of weekday-weekend ozone: importance of biogenic volatile organic compound emissions in the semi-arid southwest USA. *Atmospheric Environment* **2000**, *34*, 3445–3451.

[48] Kessler, A.; Halitschke, R.; Diezel, C.; Baldwin, I. Priming of plant defense responses in nature by airborne signaling between Artemisia tridentata and Nicotiana attenuata. *Oecologia* **2006**, *148*, 280–292.

[49] Preston, C.; Laue, G.; Baldwin, I. Methyl jasmonate is blowing in the wind, but can it act as a plant-plant airborne signal? *Biochemical systematics and ecology* **2001**, *29*, 1007–1023.

[50] Geron, C.; Guenther, A.; Greenberg, J.; Karl, T.; Rasmussen, R. Biogenic volatile organic compound emissions from desert vegetation of the southwestern US. *Atmospheric Environment* **2006**, *40*, 1645–1660.

[51] Sorooshian, A.; Wonaschuetz, A.; Jarjour, E. G.; Hashimoto, B. I.; Schichtel, B. A.; Betterton, E. A. An aerosol climatology for a rapidly growing arid region (southern Arizona): Major aerosol species and remotely sensed aerosol properties. *Journal of Geophysical Research-Atmospheres* **2011**, *116*, D19205.

[52] Jardine, K.; Abrell, L.; Kurc, S. A.; Huxman, T.; Ortega, J.; Guenther, A. Volatile organic compound emissions from Larrea tridentata (creosotebush). *Atmospheric Chemistry and Physics* **2010**, *10*, 12191–12206.

[53] Kanakidou, M. et al. Organic aerosol and global climate modelling: a review. *Atmospheric Chemistry and Physics* **2005**, *5*, 1053–1123.

[54] Matsunaga, S. N.; Guenther, A. B.; Potosnak, M. J.; Apel, E. C. Emission of sunscreen salicylic esters from desert vegetation and their contribution to aerosol formation RID B-1617-2008. *Atmospheric Chemistry and Physics* **2008**, *8*, 7367–7371.

[55] McArthur, E. D.; Ott, J. E. *Potential Natural Vegetation in the 17 Conterminous Western United States*; Proceedings: of shrubland ecosystem dynamics in a changing environment; 1995; pp 16–25.

[56] Thornton, J. A.; Kercher, J. P.; Riedel, T. P.; Wagner, N. L.; Cozic, J.; Holloway, J. S.; Dube, W. P.; Wolfe, G. M.; Quinn, P. K.; Middlebrook, A. M.; Alexander, B.; Brown, S. S. A large atomic chlorine source inferred from mid-continental reactive nitrogen chemistry. *Nature* **2010**, *464*, 271–274.

[57] Finlayson-Pitts, B. J.; Pitts, J. N. *Chemistry of the upper and lower atmosphere: theory, experiments, and applications*; Academic Press: San Diego, CA, USA, 2000; Chapter Rates and Mechanisms of Gas-Phase Reactions in Irradiated Organic–NO_x–Air Mixtures, pp 179–264.

[58] Helmig, D.; Klinger, L.; Guenther, A.; Vierling, L.; Geron, C.; Zimmerman, P. Biogenic volatile organic compound emissions (BVOCs) I. Identifications from three continental sites in the US. *Chemosphere* **1999**, *38*, 2163–2187.

[59] Hamilton, E. J. Water-Vapor Dependence of Kinetics of Self-Reaction of HO2 in Gas-Phase. *Journal of Chemical Physics* **1975**, *63*, 3682–3683.

[60] Cox, R. A.; Burrows, J. P. Kinetics and Mechanism of the Disproportionation of HO2 in the Gas-Phase. *Journal of Physical Chemistry* **1979**, *83*, 2560–2568.

[61] Demore, W. B. Reaction of HO2 with O3 and the Effect of Water-Vapor on HO2 Kinetics. *Journal of Physical Chemistry* **1979**, *83*, 1113–1118.

[62] Hamilton, E. J.; Lii, R. Dependence on H2O and on NH3 of Kinetics of Self-Reaction of HO2 in Gas-Phase Formation of HO2.H2O and HO2.NH3 Complexes. *International Journal of Chemical Kinetics* **1977**, *9*, 875–885.

[63] Kircher, C. C.; Sander, S. P. Kinetics and Mechanism of HO2 and DO2 Disproportionations. *Journal of Physical Chemistry* **1984**, *88*, 2082–2091.

[64] Lii, R. R.; Gorse, R. A.; Sauer, M. C.; Gordon, S. Temperature-Dependence of the Gas-Phase Self-Reaction of HO2 in the Presence of NH3. *Journal of Physical Chemistry* **1980**, *84*, 813–817.

[65] Sander, S. P.; Peterson, M.; Watson, R. T.; Patrick, R. Kinetics Studies of the HO2 + HO2 and DO2 + DO2 Reactions at 298-K. *Journal of Physical Chemistry* **1982**, *86*, 1236–1240.

[66] Kanno, N.; Tonokura, K.; Tezaki, A.; Koshi, M. Water dependence of the HO2 self reaction: Kinetics of the HO2-H2O complex. *Journal of Physical Chemistry a* **2005**, *109*, 3153–3158.

[67] English, A. M.; Hansen, J. C.; Szente, J. J.; Maricq, A. M. The effects of water vapor on the CH3O2 self-reaction and reaction with HO2. *Journal of Physical Chemistry a* **2008**, *112*, 9220–9228.

[68] Voehringer-Martinez, E.; Hansmann, B.; Hernandez, H.; Francisco, J. S.; Troe, J.; Abel, B. Water catalysis of a radical-molecule gas-phase reaction. *Science* **2007**, *315*, 497–501.

[69] Long, B.; jun Zhang, W.; feng Tan, X.; wen Long, Z.; bo Wang, Y.; sen Ren, D. Theoretical Study on the Gas Phase Reaction of Sulfuric Acid with Hydroxyl Radical in the Presence of Water. *Journal of Physical Chemistry a* **2011**, *115*, 1350–1357.

[70] Clark, J.; English, A. M.; Hansen, J. C.; Francisco, J. S. Computational study on the existence of organic peroxy radical-water complexes (RO2 center dot H2O). *Journal of Physical Chemistry a* **2008**, *112*, 1587–1595.

[71] Kanno, N.; Tonokura, K.; Koshi, M. Equilibrium constant of the HO2-H2O complex formation and kinetics of HO2+HO2-H2O: Implications for tropospheric chemistry. *Journal of Geophysical Research-Atmospheres* **2006**, *111*, D20312.

[72] Aloisio, S.; Francisco, J. Existence of a hydroperoxy and water (HO2 center dot H2O) radical complex. *Journal of Physical Chemistry a* **1998**, *102*, 1899–1902.

[73] Sawada, S.; Totsuka, T. Natural and anthropogenic sources and fate of atmospheric ethylene. *Atmospheric Environment* **1986**, *20*, 821–832.

[74] Finlayson-Pitts, B. J.; Pitts, J. N. *Chemistry of the upper and lower atmosphere: theory, experiments, and applications*; Academic Press: San Diego, CA, USA, 2000; Chapter Laboratory techniques for determining relative rate constants for gas-phase reactions, pp 149–150.

[75] Atkinson, R.; Aschmann, S. M. Kinetics of the Gas-Phase Reaction of Cl Atoms with a Series of Organics at 296+/- 2k and Atmospheric-Pressure. *International Journal of Chemical Kinetics* **1985**, *17*, 33–41.

[76] THORLABS, LED370E Specifications and Documentation.

[77] Frisch, M. J. et al. Gaussian 09 Revision A.1. Gaussian, Inc. Wallingford CT 2009.

[78] McQuarrie, D. A.; Simon, J. D. *Physical Chemistry: A Molecular Approach*, 1st ed.; University Science Books, 1997.

[79] Steinfeld, J. I.; Francisco, J. S.; Hase, W. L. *Chemical Kinetics and Dynamics*; Prentice Hall: New York, 1989.

[80] McClurg, R.; Flagan, R.; Goddard, W. The hindered rotor density-of-states interpolation function. *Journal of Chemical Physics* **1997**, *106*, 6675–6680.

[81] Chameides, W.; Lindsay, R.; Richardson, J.; Kiang, C. The Role of Biogenic Hydrocarbons in Urban Photochemical Smog - Atlanta as a Case-Study. *Science* **1988**, *241*, 1473–1475.

[82] Andersen, V. F.; Wallington, T. J.; Nielsen, O. J. Atmospheric Chemistry of i-Butanol. *Journal of Physical Chemistry A* **2010**, *114*, 12462–12469.

[83] Imamura, T.; Iida, Y.; Obi, K.; Nagatani, I.; Nakagawa, K.; Patroescu-Klotz, J.; Hatakeyama, S. Rate coefficients for the gas-phase reactions of OH radicals with methylbutenols at 298 K. *International Journal of Chemical Kinetics* **2004**, *36*, 379–385.

[84] Wallington, T. J.; Hurley, M. D. Atmospheric chemistry of hexafluorocyclobutene, octafluorocyclopentene, and hexafluoro-1,3-butadiene. *Chemical Physics Letters* **2011**, *507*, 19–23.

[85] Bowman, J.; Barket, D.; Shepson, P. Atmospheric chemistry of nonanal. *Environmental science and technology* **2003**, *37*, 2218–2225.

[86] Gratien, A.; Johnson, S. N.; Ezell, M. J.; Dawson, M. L.; Bennett, R.; Finlayson-Pitts, B. J. Surprising Formation of p-Cymene in the Oxidation of alpha-Pinene in Air by the Atmospheric Oxidants OH, O(3), and NO(3). *Environmental science and technology* **2011**, *45*, 2755–2760.

Appendix A

$OH^{\cdot}$ radical source

In many previous studies (e.g.[43,82–84]), methyl nitrite has been used as the $OH^{\cdot}$ radical source by the following reactions,

$$CH_3ONO + h\nu \longrightarrow CH_3O^{\cdot} + NO \tag{A.1}$$

$$CH_3O^{\cdot} + O_2 \longrightarrow HCHO + HO_2^{\cdot} \tag{A.2}$$

$$HO_2^{\cdot} + NO \longrightarrow OH^{\cdot} + NO_2 \tag{A.3}$$

Other nitrites (in particular isopropyl nitrite[85,86]) follow a similar reaction scheme, also leading to the formation of $OH^{\cdot}$. Methyl nitrite and isopropyl nitrite are not easily purchased and therefore often must be synthesized. Butyl nitrite (95%) can be purchased from Sigma Aldrich and can also be used to form $OH^{\cdot}$ radical by photolysis with 375 nm light and subsequent reaction with O_2 and NO. However, this method was not used in the relative rates experiments with thujone because thujone does not have a unique absorption feature in the presence of butyl nitrite and its degradation products.

Appendix B

MATLAB code for relative rates experiments

B.1 Reading data from *.csv files

The function `readRRdata` reads the spectra (in *.csv format) saved in `folder` (the folder name should be the month and date, for example "Nov3") assuming the files are named with the date and time of when they were collected. The function averages the signal between 1757 cm^{-1} and 1767 cm^{-1} (excluding the data between 1761 cm^{-1} and 1763 cm^{-1}) in each spectrum and returns the vector containing these points in `ATh` (data points for thujone). Similarly, the average absorption between 3032 cm^{-1} and 3042 cm^{-1} in each spectrum is saved and returned in the vector `ATo` (data points for toluene). The vector `time` is returned with the times corresponding to the data points in `ATh` and `ATo`.

```
function [time, ATh, ATo] = readRRdata(folder,year)

% Read data in folder (folder name is the date when the expermiment was
% started)

[num,day1] = weekday(strcat(folder,',',year));

files = dir(strcat(folder,'/*.CSV'));

n = length(files);

[filenames{1:n}] = deal(files.name);
t = zeros(n,1);
peakTh = zeros(n,1);
```

```
peakTo = zeros(n,1);

%import the first set of data
data = csvread(strcat(folder,'/',filenames{1}));

%index each peak
Th_ind = (data(:,1) > 1757 & data(:,1) < 1761) | ...
    (data(:,1) > 1763 & data(:,1) < 1767);   %thujone
To_ind = data(:,1) > 3032 & data(:,1) < 3042;   %toluene
% To_ind = data(:,1) > 1598 & data(:,1) < 1610;   %toluene

%record the time for each file and read each data file and find each peak
for ii = 1:n
    time = filenames{ii}(12:19);
    d = ~strcmp(filenames{ii}(1:3),day1);
    h = str2double(time(1:2));
    m = str2double(time(4:5));
    s = str2double(time(7:8));
    t(ii) = 60^2*(d*24+h)+60*m+s;

    data = csvread(strcat(folder,'/',filenames{ii}));

    peakTh(ii) = mean(data(Th_ind,2));
    peakTo(ii) = mean(data(To_ind,2));

    % Save spectra in workspace
%     time_string = strcat(filenames{ii}(1:3),time(1:2),time(4:5),time(7:8));
%     assignin('base',time_string,data);
end

clear time d h m s data

[min_val min_ind] = min(t);

time = [t(min_ind:end);t(1:min_ind-1)];             %in seconds
ATh = [peakTh(min_ind:end);peakTh(1:min_ind-1)];
```

```
ATo = [peakTo(min_ind:end);peakTo(1:min_ind-1)];
```

B.2 Analyzing relative rates data

The function `analyzeRRdata` accepts the folder name and the output of `readRRdata` as well as optional inputs specifying which data point should be used for t_0 and where the data should be truncated. The function fits the data to the equation,

$$\ln \frac{[\mathrm{X}_1]_0}{[\mathrm{X}_1]_t} = \beta_1 + \beta_2 \ln \frac{[\mathrm{X}_2]_0}{[\mathrm{X}_2]_t} + \beta_3 t \tag{B.1}$$

$$= \beta_1 + \frac{k_1}{k_2} \ln \frac{[\mathrm{X}_2]_0}{[\mathrm{X}_2]_t} + \mathcal{F}\sigma\Phi t \tag{B.2}$$

and returns the vector `RRphotobeta` containing the coefficients $[\beta_1\ \beta_2\ \beta_3]$ where β_1 is equal to the y-intercept, β_2 is equal to k_1/k_2, and β_3 is equal to $\mathcal{F}\sigma\Phi$. The function also returns the standard deviation for each of the β values in `RRphotosm`. The function also fits the data to the basic relative rates model,

$$\ln \frac{[\mathrm{X}_1]_0}{[\mathrm{X}_1]_t} = \beta_1 + \beta_2 \ln \frac{[\mathrm{X}_2]_0}{[\mathrm{X}_2]_t} \tag{B.3}$$

$$= \beta_1 + \frac{k_1}{k_2} \ln \frac{[\mathrm{X}_2]_0}{[\mathrm{X}_2]_t} \tag{B.4}$$

and returns the vector `RRbeta` containing the coefficients $[\beta_1\ \beta_2]$ where β_1 is equal to the y-intercept and β_2 is equal to k_1/k_2 and the vector `RRphotosm` containing the standard deviations for each of the β values. Although in both relative rates models the fit should intercept the origin, the y-intercept is allowed to vary here in order to account for any error in the measurement of $[\mathrm{X}_1]_0$ and $[\mathrm{X}_2]_0$.

```
function [RRphotobeta RRphotosm RRbeta RRsm n] = analyzeRRdata(folder,...
    time,ATh,ATo,varargin)
```

```
if ~isempty(varargin)
    tf = varargin{1};
    t0ind = varargin{2};
else
    tf = 10000;
    t0ind = 2;
end

time = time(t0ind:end);
ATh = ATh(t0ind:end);
ATo = ATo(t0ind:end);

dt = diff(time);
ind = find(dt < 350);
t0ind2 = ind(1);

[dnu t0ind3] = max(ATh);

[dnu t0ind4] = max(ATo);

t0ind = max([1,t0ind2,t0ind3,t0ind4]);

t0 = time(t0ind);

tplot = time(t0ind:end)-t0;

AThplot = ATh(t0ind:end);

AToplot = ATo(t0ind:end);

% tf = min(tf,10000);
tf = min(tf,5400);

tplot = tplot(tplot < tf);
AThplot = AThplot(tplot < tf);
AToplot = AToplot(tplot < tf);
```

```
% To make figure for paper and presentation
figure,
subplot(1,2,1)
plot(tplot/3600,AThplot/(1e-3),'.k')
title('A')
xlabel('time (h)')
ylabel('Absorbance/10^{-3}')

subplot(1,2,2)
plot(tplot/3600,AToplot/(1e-3),'.k')
title('B')
xlabel('time (h)')
ylabel('Absorbance/10^{-3}')

% fit to relative rates model correcting for photolysis of thujone
tplot = tplot - tplot(1);
tplot = tplot/3600;   %hours

del = AToplot <= 0 | AThplot <= 0;

tplot(del) = [];
AToplot(del) = [];
AThplot(del) = [];

lnx2 = log(AToplot(1)./AToplot);
lnx1 = log(AThplot(1)./AThplot);

X2photo = [lnx2 tplot];

RRphotostats = regstats(lnx1,X2photo);
RRphotobeta = RRphotostats.beta;
RRphotosm = sqrt(diag(RRphotostats.covb));

% fit to simple relative rates model
X2 = lnx2;
```

```
RRstats = regstats(lnx1,X2);
RRbeta = RRstats.beta;
RRsm = sqrt(diag(RRstats.covb));

% To make figure for paper and presentation
figure,
plot(lnx2,lnx1,'.k')
hold on
plot(lnx2,RRstats.yhat,'-k','LineWidth',1)
plot(lnx2,lnx1 - RRphotobeta(3)*tplot,'xk','MarkerSize',8)
[lnx2 ind] = sort(lnx2);
plot(lnx2,RRphotostats.yhat(ind) - RRphotobeta(3)*tplot(ind),'--k','LineWidth',1)
xlabel('ln([Tolulene]_0/[Tolulene]_t)')
ylabel('ln([Thujone]_0/[Thujone]_t)')
legend('Data','Fit with basic relative rates model',...
    'Data corrected for photolysis',...
    'Fit with photolysis relative rates model','Location','NorthWest')

disp(strcat(folder,' (photolysis)'))
disp('[yint k1/k2 FsigmaPhi]')
disp(RRphotobeta')
disp(RRphotosm');
disp(strcat(folder,' (no photolysis)'))
disp('[yint k1/k2 FsigmaPhi]')
disp(RRbeta')
disp(RRsm');

n = length(tplot);
```

Appendix C

MATLAB code for calculating the equilibrium constant for β-HEP·H_2O complex formation

This script uses data in a MATLAB workspace saved as `logdata.mat` and the function `calculateK` to calculate the equilibrium constant for β-HEP·H_2O complex formation as described in chapter 3. The function `calculateK` returns the calculated equilibrium constants in `K` at each of the temperatures in `T` as well as an array (`percent`) containing the experimental temperatures, the equilibrium constant at those temperatures, the experimental water vapor concentrations, and the percent of β-HEP complexed under those experimental conditions. For comparison, the equilibrium constant and percent of β-HEP complexed is also calculated using only the harmonic oscillator model for the vibrational partition function (`KHO` and `percentHO`).

The script is given below.

```
clear all
close all
clc

h = 6.62608e-34;      % J s
kb = 1.38065e-23;     % J/K
c = 2.99792458e10;    % cm/s
NA = 6.02214e23;      % 1/mol
R = 1.987207e-3;      % kcal/mol/K
Hbond = 2;            % kcal/mol
mH = 1.00794;         % amu
mH = mH/NA/1000;      % kg
```

```
mO = 15.9994;        % amu
mO = mO/NA/1000;     % kg
mC = 12.0107;        % amu
mC = mC/NA/1000;     % kg

% Read data from log files

log = load('logdata');
rotHEP1 = log.rotHEP1;
rotHEP2 = log.rotHEP2;
rotC244 = log.rotC244;
rotC248 = log.rotC248;
rotC256 = log.rotC256;
HEP1log = log.HEP1log;
HEP2log = log.HEP2log;
C244log = log.C244log;
C248log = log.C248log;
C256log = log.C256log;
HEP1logo = log.HEP1logo;
HEP2logo = log.HEP2logo;
C244logo = log.C244logo;
C248logo = log.C248logo;
C256logo = log.C256logo;
XC244 = log.XC244;
XC248 = log.XC248;
XC256 = log.XC256;
XHEP1 = log.XHEP1;
XHEP2 = log.XHEP2;
modelC244 = log.modelC244;
modelC248 = log.modelC248;
modelC256 = log.modelC256;
modelHEP1 = log.modelHEP1;
modelHEP2 = log.modelHEP2;

% Vibrational models
modelsHEP = [modelHEP1 modelHEP2];
```

```
modelsCOMP = [modelC244 modelC248 modelC256];

% Rotational constants
rotHEP = [rotHEP1; rotHEP2];
rotCOMP = [rotC244; rotC248; rotC256];

% Energies of individual molecules

Har2kcal = 627.509469; % (kcal/mol)/(Hartrees/particle)

EHEP1 = -304.0749019;               % Hartrees/particle
zeroHEP1 = 0.076152;                % Hartrees/particle
% EHEP1 = EHEP1 + zeroHEP1;           % Hartrees/particle
EHEP1 = EHEP1 * Har2kcal;           % kcal/mol

EHEP2 = -304.0767151;               % Hartrees/particle
zeroHEP2 = 0.076551;                % Hartrees/particle
% EHEP2 = EHEP2 + zeroHEP2;           % Hartrees/particle
EHEP2 = EHEP2 * Har2kcal;           % kcal/mol

EH2O = -76.2739028;                 % Hartrees/particle
zeroH2O = 0.021227;                 % Hartrees/particle
% EH2O = EH2O + zeroH2O;              % Hartrees/particle
EH2O = EH2O * Har2kcal;             % kcal/mol

ECOMP244 = -380.36233;              % Hartrees/particle
zeroCOMP244 = 0.100397;             % Hartrees/particle
% ECOMP244 = ECOMP244 + zeroCOMP244;  % Hartrees/particle
ECOMP244 = ECOMP244 * Har2kcal;     % kcal/mol

ECOMP248 = -380.3625218;            % Hartrees/particle
zeroCOMP248 = 0.101051;             % Hartrees/particle
% ECOMP248 = ECOMP248 + zeroCOMP248;  % Hartrees/particle
ECOMP248 = ECOMP248 * Har2kcal;     % kcal/mol

ECOMP256 = -380.3627475;            % Hartrees/particle
```

```
zeroCOMP256 = 0.100924;             % Hartrees/particle
% ECOMP256 = ECOMP256 + zeroCOMP256;  % Hartrees/particle
ECOMP256 = ECOMP256 * Har2kcal;     % kcal/mol

EHEP = [EHEP1 EHEP2];
ECOMP = [ECOMP244 ECOMP248 ECOMP256];

T = [200:350]';      % K

mHEP = 2*mC + 5*mH + 3*mO; % kg
mH2O = 2*mH + mO;    % kg
mCOMP = mHEP + mH2O; % kg

massHEP = [mHEP mH2O mCOMP];

% fundamental frequencies (anharmonic oscillator)
vibHEP1af = HEP1log(:,2);
vibHEP2af = HEP2log(:,2);
vibC244af = C244log(:,2);
vibC248af = C248log(:,2);
vibC256af = C256log(:,2);


vibanharmHEP = [vibHEP1af vibHEP2af];
vibanharmCOMP = [vibC244af vibC248af vibC256af];

% % first overtone frequencies (anharmonic oscillator)
% vibHEP1ao = HEP1logo(:,2);
% vibHEP2ao = HEP2logo(:,2);
% vibC244ao = C244logo(:,2);
% vibC248ao = C248logo(:,2);
% vibC256ao = C256logo(:,2);

% fundamental frequencies (harmonic oscillator)
vibHEP1hf = HEP1log(:,1);
vibHEP2hf = HEP2log(:,1);
```

```
vibC244hf = C244log(:,1);
vibC248hf = C248log(:,1);
vibC256hf = C256log(:,1);

vibharmHEP = [vibHEP1hf vibHEP2hf];
vibharmCOMP = [vibC244hf vibC248hf vibC256hf];

% X matrix
XHEP = [XHEP1 XHEP2];
XCOMP = [XC244 XC248 XC256];

[T K KHO percent percentHO] = calculateK(T,massHEP,rotHEP,rotCOMP,...
    EHEP,EH2O,ECOMP,vibharmHEP,vibharmCOMP,vibanharmHEP,vibanharmCOMP,...
    XHEP,XCOMP,modelsHEP,modelsCOMP);
```

The function, `calculateK` is given below.

```
function [T K KHO percent percentHO] = ...
    calculateK(T,mass,rotA,rotCOMP,EA,EH2O,ECOMP,...
    vibharmA,vibharmCOMP,vibanharmA,vibanharmCOMP,XA,XCOMP,...
    modelsA,modelsCOMP)

% NOTES: A is the peroxy radical, COMP is the complex
%   Energies should be given in kcal/mol
%   All frequencies and rotational constants should be given in cm-1
%   Masses should be given in kg

% Input:
% T: column vector containing temperatures for K calculations
% mass: row vector containing the masses of the compounds [A H2O COMP]
% rotA: matrix containing row vectors of the rotational constants for the
% different geometries of A
% rotCOMP: matrix containing row vectors of the rotational constants for
% the different geometries of the complex
```

```
% EA: row vector containing the energies of the different geometries of A
% ECOMP: row vector containing the energies of the different geometries of
% the complex
% vibharmA: matrix containing column vectors of the harmonic
% frequencies for the different geometries of A
% vibharmCOMP: matrix containing column vectors of the harmonic
% frequencies for the different geometries of the complex
% vibanharmA: matrix containing column vectors of the anharmonic
% frequencies for the different geometries of A
% vibanharmCOMP: matrix containing column vectors of the anharmonic
% frequencies for the different geometries of the complex
% XA: matrix containing column vectors of the diagonal entries of the X
% matrix for each of the geometries of A
% XCOMP: matrix containing column vectors of the diagonal entries of the X
% matrix for each of the geometries of COMP
% modelsA: a cell array containing the models used to calculate the
% vibrational partition functions. Each column corresponds to a different
% geometry of A
% modelsCOMP: a cell array containing the models used to calculate the
% vibrational partition functions. Each column corresponds to a different
% geometry of the complex

nT = length(T);

% number of geometries of A, COMP
nA = length(EA);
nCOMP = length(ECOMP);

% From Cline et al.
% Water concentrations at each temperature (274 K, 280 K, 288 K, 296 K)
H2O274 = [0.18; 1.57; 2.60; 3.32];
H2O274 = H2O274*1e16;
H2O280 = [0.29; 2.10; 4.70; 5.86; 6.76];
H2O280 = H2O280*1e16;
H2O288 = [0.20; 3.80; 8.21; 12.20];
H2O288 = H2O288*1e16;
```

```
H2O296 = [0.18; 6.26; 11.80; 22.50];
H2O296 = H2O296*1e16;

% Define variables
global h kb c NA R Hbond mH mO

h = 6.62608e-34;     % J s
kb = 1.38065e-23;    % J/K
c = 2.99792458e10;   % cm/s
NA = 6.02214e23;     % 1/mol
R = 1.987207e-3;     % kcal/mol/K
Hbond = 2;           % kcal/mol
mH = 1.00794;        % amu
mH = mH/NA/1000;     % kg
mO = 15.9994;        % amu
mO = mO/NA/1000;     % kg

mA = mass(1); % kg
mH2O = mass(2);    % kg
mCOMP = mass(3); % kg

% Calculate q_trans/V
H2OqT = qtrans(mH2O,T);
AqT = qtrans(mA,T);
COMPqT = qtrans(mCOMP,T);

AqR = zeros(nT,nA);
COMPqR = zeros(nT,nCOMP);

% Calculate q_rot
for jj = 1:nA
    AqR(:,jj) = qrot(rotA(jj,:),1,T);
end
for jj = 1:nCOMP
    COMPqR(:,jj) = qrot(rotCOMP(jj,:),1,T);
end
```

```
% Calculate q_vib
AqV = zeros(nT,nA);
AqVHO = zeros(nT,nA);
COMPqV = zeros(nT,nCOMP);
COMPqVHO = zeros(nT,nCOMP);
for jj = 1:nA
    [AqV(:,jj) AqVHO(:,jj)] = qvibmodels(modelsA(:,jj),vibharmA(:,jj),...
        vibanharmA(:,jj),XA(:,jj),T);
end
for jj = 1:nCOMP
    [COMPqV(:,jj) COMPqVHO(:,jj)] = qvibmodels(modelsCOMP(:,jj),...
        vibharmCOMP(:,jj),vibanharmCOMP(:,jj),XCOMP(:,jj),T);
end

% Calculate K

% Use rotational/vibrational partition function for water from
% Partridge/Schwenke paper
coef = [11.31703303; -3.651093415; 0.47443849; 0.007443446; 0.000544827];
Tmat2 = [ones(nT,1) T.^(1/2) T T.^(3/2) T.^2];

% Calculate the partition function for water (excluding the electronic
% partition function)
% divide by 4 to correct for nuclear spin states of protons
qH2O = 0.25*(Tmat2*coef).*H2OqT;

% Calculate q_elec for A and complex (with correction factors)
EcA = min(EA);

EAc = EA - EcA;
AqE = 2*exp(-(ones(nT,1)*EAc)./(R*(T*ones(1,nA))));

qA = AqR.*AqV.*AqE;

EcCOMP = min(ECOMP);
```

```
ECOMPc = ECOMP - EcCOMP;
COMPqE = 2*exp(-(ones(nT,1)*ECOMPc)./(R*(T*ones(1,nCOMP))));

qCOMP = COMPqR.*COMPqV.*COMPqE;

K = COMPqT.*(sum(qCOMP,2))./(AqT.*(sum(qA,2)).*qH2O)...
    .*exp(ones(nT,1)*(EcA + EH2O - EcCOMP)./(R*T));


% Calculate [Complex]/[RO2] ratio

K274 = K(T == 274);
ratio274 = K274*H2O274;
percent274 = 1./(1./ratio274 + 1)*100;
K280 = K(T == 280);
ratio280 = K280*H2O280;
percent280 = 1./(1./ratio280 + 1)*100;
K288 = K(T == 288);
ratio288 = K288*H2O288;
percent288 = 1./(1./ratio288 + 1)*100;
K296 = K(T == 296);
ratio296 = K296*H2O296;
percent296 = 1./(1./ratio296 + 1)*100;

figure,
plot(1./T,log10(K))
hold on
axis([3e-3 5e-3 -21 -18])
xlabel('1/T')
ylabel('log_{10}(K)')

percent  = [274*ones(length(H2O274),1),K274*ones(length(H2O274),1),...
    H2O274/1e16,percent274;
            280*ones(length(H2O280),1),K280*ones(length(H2O280),1),...
            H2O280/1e16,percent280;
```

```
            288*ones(length(H2O288),1),K288*ones(length(H2O288),1),...
            H2O288/1e16,percent288;
            296*ones(length(H2O296),1),K296*ones(length(H2O296),1),...
            H2O296/1e16,percent296];


% Calculate K with harmonic oscillator vibrational partition functions

qAHO = AqR.*AqVHO.*AqE;

qCOMPHO = COMPqR.*COMPqVHO.*COMPqE;

KHO = COMPqT.*(sum(qCOMPHO,2))./(AqT.*(sum(qAHO,2)).*qH2O)...
    .*exp(ones(nT,1)*(EcA + EH2O - EcCOMP)./(R*T));


% Calculate [Complex]/[RO2] ratio using KHO

K274HO = KHO(T == 274);
ratio274HO = K274HO*H2O274;
percent274HO = 1./(1./ratio274HO + 1)*100;
K280HO = KHO(T == 280);
ratio280HO = K280HO*H2O280;
percent280HO = 1./(1./ratio280HO + 1)*100;
K288HO = KHO(T == 288);
ratio288HO = K288HO*H2O288;
percent288HO = 1./(1./ratio288HO + 1)*100;
K296HO = KHO(T == 296);
ratio296HO = K296HO*H2O296;
percent296HO = 1./(1./ratio296HO + 1)*100;

plot(1./T,log10(KHO),'r')
legend('Multiple models', 'Harmonic oscillator',...
    'Location','NorthWest')

percentHO = [274*ones(length(H2O274),1),K274HO*ones(length(H2O274),1),...
```

```
    H2O274/1e16,percent274HO;
            280*ones(length(H2O280),1),K280HO*ones(length(H2O280),1),...
            H2O280/1e16,percent280HO;
            288*ones(length(H2O288),1),K288HO*ones(length(H2O288),1),...
            H2O288/1e16,percent288HO;
            296*ones(length(H2O296),1),K296HO*ones(length(H2O296),1),...
            H2O296/1e16,percent296HO];

function qT = qtrans(m,T)

    % Calculate the translational partition function for a molecule

    % m is the mass of the molecule (in kg)
    % T is a nT-by-1 array containing temperatures (K)
    % returns qT = q_trans/V

    lambda = h./((2*pi*m*kb*T).^(0.5));
    qT = 1./(lambda.^3)*100^(-3);       % 1/cm^3

end



function qR = qrot(rot,sigma,T)

    % Calculate the rotational partition function for a molecule

    % rot is a vector of the rotational constants in units of cm^-1
    % sigma is the symmetry number for the molecule
    % T is a nT-by-1 array containing temperatures (K)

    qR = 1/sigma*(kb*T/(h*c)).^(1.5)*(pi/prod(rot))^(0.5);

end
```

```
function [qviballmodels qvibHO] = qvibmodels(model,vibharm,...
        vibanharmfund,X,T)
% function [qviballmodels qvibHO] = qvibmodels(model,vibharm,...
%         vibanharmfund,vibanharmover,X,T)

    % Calculate the vibrational partition function at each temperature in T
    % by applyin the model approximation that most accurately reflects the
    % motion of the vibrational mode

    % INPUT
    % model is a nmodes-by-1 array listing the model that best represents
    %       each vibrational mode
    % vibharm is a nmodes-by-1 array of the harmonic frequencies for each
    %       vibrational mode
    % vibanharmfund is a nmodes-by-1 array of the anharmonic frequencies
    %       for each vibrational mode
    % X is a nmodes-by-1 array containing the diagonal entries of the X
    %       matrix (in cm^-1)
    % T is a nT-by-1 array containing temperatures (K)

    % OUTPUT
    % qviballmodels returns an nT-by-1 array with the vibrational partition
    %   function calculated at each temperature where the partition
    %   function for each mode was calculated by the model specified in the
    %   "model" input
    % qvibHO returns an nT-by-1 array with the vibrational partition
    %   function calculated at each temperature where the partition
    %   function for each mode was calculated using the harmonic oscillator
    %   (with anharmonic frequencies)

    % Use codes in the model array to find the modes characterized by each
    % model

    M = strcmpi(model,'Morse');
    M1 = strcmpi(model,'Morse1');
```

```
    M2 = strcmpi(model,'Morse2');
    HO = strcmpi(model,'HO');
    HR1 = strncmpi(model,'HR1',3);
    HR2 = strncmpi(model,'HR2',3);

    if any(~(M | M1 | M2 | HO | HR1 | HR2))
        error(['At least one vibrational mode does not have an ',...
            'assigned model'])
    end

    % Calculate the partition functions for the modes characterized by the
    % Morse oscillator
    qvibM = qvibMorse(vibharm(M),X(M),T);
%   qvibM = qvibMorse(vibharm(M),vibanharmfund(M),vibanharmover(M),X(M),T);
    qvibM1 = qvibMorseHbond(vibharm(M1),T,1);
    qvibM2 = qvibMorseHbond(vibharm(M2),T,2);

    % Calculate the partition functions for all modes using the harmonic
    % oscillator (with anharmonic frequencies)
    qvibHOall = qvibHarm(vibanharmfund,T);
    % Isolate the modes that were specified as Harmonic Oscillator modes
    % in "model"
    qvibHO = qvibHarm(vibharm(HO),T);
%     qvibHO = qvibHOall(:,HO);

    % Calculate the partition functions for the modes characterized by the
    % hindered rotor model
    % Calculate the moments of inertia for the hindered rotors
    OHlength = 0.95;            % Angstroms
    OHlength = OHlength*1e-8;   % cm
    OOlength = 1.5;             % Angstroms
    OOlength = OOlength*1e-8;   % cm
    COHangle = 105*pi/180;      % radians
    COOangle = 120*pi/180;      % radians
    HOHangle = 104.5*pi/180;    % radians
```

```
ICOH = mH*(OHlength*sin(pi - COHangle))^2;
ICOO = mO*(OOlength*sin(pi - COOangle))^2;
IHOH1 = mH*(OHlength*sin(pi - HOHangle))^2;
IHOH2 = 2*mH*OHlength^2;
IHOHCOH = mH*(OHlength*sin(pi - HOHangle))^2 + ...
    mH*(OHlength*sin(pi - COHangle))^2;

% Assign the moments of inertia to the vibrational modes
modelHR1 = model(HR1);
IHR1 = zeros(1,length(modelHR1));
HR1COH = strcmpi(modelHR1,'HR1COH');
IHR1(HR1COH) = ICOH;
HR1COO = strcmpi(modelHR1,'HR1COO');
IHR1(HR1COO) = ICOO;
HR1HOH1 = strcmpi(modelHR1,'HR1HOH1');
IHR1(HR1HOH1) = IHOH1;
HR1HOH2 = strcmpi(modelHR1,'HR1HOH2');
IHR1(HR1HOH2) = IHOH2;
HR1HOHCOH = strcmpi(modelHR1,'HR1HOHCOH');
IHR1(HR1HOHCOH) = IHOHCOH;

modelHR2 = model(HR2);
IHR2 = zeros(1,length(modelHR2));
HR2HOHCOH = strcmpi(modelHR2,'HR2HOHCOH');
IHR2(HR2HOHCOH) = IHOHCOH;

if any(IHR1 == 0) || any(IHR2 == 0)
    error(['At least one vibration does not have an assigned ',...
    'moment of inertia'])
end

qvibHR1 = qvibHinderedRotor(vibharm(HR1),IHR1,T,1);
qvibHR2 = qvibHinderedRotor(vibharm(HR2),IHR2,T,2);

% Concatenate all calculated partition functions in a single
% nT-by-nmodes array
```

```
    qviballmodelsmat = [qvibM qvibM1 qvibM2 qvibHO qvibHR1 qvibHR2];

    qviballmodelsmat(:,vibharm <= 0 | vibanharmfund <= 0) = 1;

    % Find the product of the vibrational partition functions for all
    % vibrational modes to find the overall vibrational partition function
    % for the molecule at each temperature
    qviballmodels = prod(qviballmodelsmat,2);

    % Calculate the overall harmonic oscillator partition function for the
    % molecule at each temperature
    qvibHOall(:,vibharm <= 0 | vibanharmfund <= 0) = 1;
    qvibHO = prod(qvibHOall,2);

end



function q = qvibHarm(vib,T)

    % Calculate the vibrational partition function based on the Harmonic
    % Oscillator model (using the anharmonic frequencies for each mode)

% vib is a nmodes-by-1 array containing the anharmonic frequencies
%       corresponding to each vibrational mode (cm^-1)
    % T is a nT-by-1 array containing temperatures (K)

    nT = length(T);

    Tmat = T*ones(1,length(vib));
    freqmat = ones(nT,1) * vib';
    calc1 = exp(-h*c*freqmat./(kb*Tmat));
    q = 1./(1-calc1);

end
```

```
function q = qvibMorse(nue,xe,T)

    % Calculate the vibrational partition function using the Morse
    % oscillator with the values for the parameters based on the
    % diagonal entry in the X matrix corresponding to the vibrational mode

    % nue is a nmodes-by-1 array containing the harmonic vibrational
    %       energies corresponding to each vibrational mode (cm^-1)
    % xe is a nmodes-by-1 array containing the diagonal entries of the X ]
    %       matrix (cm^-1)
    % T is a nT-by-1 array containing temperatures (K)

    nT = length(T);
    nmodes = length(nue);

    q = zeros(nT,nmodes);

    % Calculate the maximum possible vibrational quantum number (vmax) and
    % the number of vibrational states that will be occupied (N)
    vstar = -0.5*nue./xe - 0.5;
    vmax = floor(vstar);
    N = vmax + 1;

    for ii = 1:nmodes
        v = 0:vmax(ii);
        Tmat1 = T*ones(1,N(ii));
        Gv = nue(ii)*(v + 0.5) + xe(ii)*(v+0.5).^2;
        dG = Gv - Gv(1);
        dGmat = ones(nT,1)*dG;
        calc1 = exp(-h*c*dGmat./(kb*Tmat1));
        q(:,ii) = sum(calc1,2);
        clear v Tmat1 Gv dG dGmat calc1
    end
```

```
end


% function q = qvibMorse(nue,anharmfund,anharmover,xemat,T)
%
%     % Calculate the vibrational partition function using the Morse
%     % oscillator with the values for the parameters based on the
%     % x value calculated from the fundamental and overtone anharmonic
%     % frequencies
%
%     % nue is a nmodes-by-1 array containing the harmonic vibrational
%     %       energies corresponding to each vibrational mode (cm^-1)
%    % xe is a nmodes-by-1 array containing the diagonal entries of the X ]
%     %       matrix (cm^-1)
%     % T is a nT-by-1 array containing temperatures (K)
%
%     nT = length(T);
%     nmodes = length(nue);
%
%     q = zeros(nT,nmodes);
%
%     xe = 0.5*(anharmover - 2*anharmfund);
%
%     % Replace the positive xe values with the corresponding diagonal
%     % entries from the X matrix
%     xe(xe > 0) = xemat(xe > 0);
%
%    % Calculate the maximum possible vibrational quantum number (vmax) and
%     % the number of vibrational states that will be occupied (N)
%     vstar = -0.5*nue./xe - 0.5;
%     vmax = floor(vstar);
%     N = vmax + 1;
%
%     % Adjust xe using integer N
%     xenew = -0.5*nue./N;     % cm-1
%
```

```
%     for ii = 1:nmodes
%         v = 0:vmax(ii);
%         Tmat1 = T*ones(1,N(ii));
%         Gv = nue(ii)*(v + 0.5) + xenew(ii)*(v+0.5).^2;
%         dG = Gv - Gv(1);
%         dGmat = ones(nT,1)*dG;
%         calc1 = exp(-h*c*dGmat./(kb*Tmat1));
%         q(:,ii) = sum(calc1,2);
%         clear v Tmat1 Gv dG dGmat calc1
%     end
%
% end


function q = qvibMorseHbond(nue,T,n)

    % Calculate the vibrational partition function using the Morse
    % oscillator with the values for the parameters based on the
    % dissociation energy for the bond equaling the strength of one
    % hydrogen bond (5.0 kcal/mol)

    % nue is a nmodes-by-1 array containing the harmonic vibrational
    %       energies corresponding to each vibrational mode (cm^-1)
    % T is a nT-by-1 array containing temperatures (K)
    % n is the number of hydrogen bonds that make up the dissociation
    %       energy

    nT = length(T);
    nmodes = length(nue);

    q = zeros(nT,nmodes);

    Dnew = n*Hbond;                 % kcal/mol
    Dnew = Dnew * 4184 / NA;    % J
    Dnew = Dnew/(h*c);          % cm-1
```

```
    %Calculate vmax and N from Dnew
    xenew = -0.25*(nue.^2)./Dnew;   % cm^-1
    N = -0.5*nue./xenew;
    N = round(N);
    vmax = N - 1;

    % Adjust xe using integer N
    xenew = -0.5*nue./N;     % cm-1

    for ii = 1:nmodes
        v = 0:vmax(ii);
        Tmat1 = T*ones(1,N(ii));
        Gv = nue(ii)*(v + 0.5) + xenew(ii)*(v+0.5).^2;
        dG = Gv - Gv(1);
        dGmat = ones(nT,1)*dG;
        calc1 = exp(-h*c*dGmat./(kb*Tmat1));
        q(:,ii) = sum(calc1,2);
        clear v Tmat1 Gv dG dGmat calc1
    end

end



function q = qvibHinderedRotor(vibharm,I,T,numHbonds)

    % Calculate the vibrational partition function using the hindered rotor
    % model as described in McClurg et al. (1997)

    % qHO is the partition function for each of the vibrational modes at
    % each temperature in T calculated using the Harmonic Oscillator model

    % I is a 1-by-nmodes array containing the moment of inertia for each of
    % the vibrational modes

    % T is a nT-by-1 array containing the temperatures at which the
```

```
    % partition functions are being calculated

    % numHbonds is the number of hydrogen bonds that are being broken and
    % formed in the hindered rotor motion (defines the barrier height in
    % the hindered rotor model)

    qHO = qvibHarm(vibharm,T);

    hbar = h/(2*pi);                % J s

    nT = length(T);
    nmodes = length(I);

    HbondJ = Hbond * 4184 / NA;        % J

    w = HbondJ*numHbonds;             % 1-by-nmodes array, units: J

    omega = sqrt(w./(2*I));          % 1/s
    omegamat = ones(nT,1)*omega;
    r = w./(hbar*omega);             % (unitless)
    rmat = ones(nT,1)*r;
    Tmat = T*ones(1,nmodes);

    theta = kb*Tmat./(hbar*omegamat);  % (unitless)
    rtheta = rmat./theta;            % (unitless)

    q = qHO.*(pi*rtheta).^0.5.*exp(-0.5*rtheta).*besseli(0,0.5*rtheta);

end

end
```